Engineering and Technology Journal
Journal homepage: https://etj.uotechnology.edu.iq

Computational insights into the thermal performance enhancement of solar air heater channel through metal foam integration

Kadhim Al-Chlaihawi[a*], **Moayed R. Hasan**[b], **Ali L. Kaied**[b]

[a] Department of Mechanical Engineering, University of Al-Qadisiyah, Al Diwaniyah, Al-Qadisiyah, 58001, Iraq .
[b] Mechanical Engineering Dept., University of Technology-Iraq, Alsina'a street, 10066 Baghdad, Iraq.
*Corresponding author Email: kadhim.idan@qu.edu.iq

HIGHLIGHTS

- Fluid flow and heat transfer in an SAH channel with metal foam were simulated
- The LTNE and DEF models were used.
- The thermo-hydraulic performance of SAH was analyzed, considering several key factors.
- Compared to the empty SAH duct, Nu rises 9-10.6 times and friction factor by 53.5-56.6 times.
- TPF varies from 2.33 to 2.82 at H_f =0.6 and ω=10 PPI.

ARTICLE INFO

Handling editor: Jalal M. Jalil

Keywords:
metal foam; local thermal non-equilibrium; model (LTNE) forced convection; TPF; SAH.

ABSTRACT

The two-dimensional numerical simulations focused on fluid flow and heat transfer within a solar air heater (SAH) channel incorporating copper metal foam with a porosity of 90% were carried out in this study. The Local Thermal Non-equilibrium (LTNE) and Darcy-Extended Forchheimer (DEF) models were employed to predict fluid and thermal transport in the partially porous SAH channel. In the free flow zone, the $k-\varepsilon$ turbulence model was utilized. The thermal and thermo-hydraulic performances of SAH were examined concerning several factors, including pore density (ω), Reynolds number (Re), and dimensionless foam height (H_f). The results demonstrate that inserting a porous substrate into the SAH can substantially increase heat transmission. This enhancement ranges from 4.4 to 18.04 times compared to an empty duct for $H_f = 0.2, 0.4, 0.6, 0.8,$ and 1 at $\omega = 10$PPI. Moreover, increased porous layer height and pore density lead to a corresponding increase in pressure drop. Evaluating both the improvement in heat transmission and the associated pressure penalty, the case with $H_f = 0.6$, $\omega = 10$ PPI, and $\mathrm{Re} = 16{,}000$ demonstrate superior overall performance, boasting a higher Thermal Performance Factor (TPF) of 2.82 when compared to an empty channel. This work presents significant findings on optimizing metal foam applications in SAH systems, offering new insights into the field.

1. Introduction

Energy plays a fundamental role in driving the survival and advancement of the human race. The twenty-first century's economic expansion and societal progress are predominantly attributable to the extensive use of conventional fossil fuel-based energy sources. However, conscientious and ecologically sound energy utilization is an enormous challenge confronting society in the twenty-first century. Energy systems have been and continue to observe a transition towards sustainable energy. The ongoing shift towards sustainable energy necessitates a greater reliance on renewable energy sources, the growth of low-carbon energy alternatives, and the advancement and implementation of technologies that reduce emissions [1,2]. This transition aims to enhance energy efficiency, reduce carbon emissions, and promote environmental sustainability. Solar energy, being a readily accessible and environmentally sustainable renewable energy source, possesses the capacity to satisfy heat demands in numerous sectors, including but not limited to residential areas, agriculture, and households. Consequently, it is crucial to diminish our dependence on conventional fossil fuels and attain our goals of embracing low-carbon energy sources [3,4].

Solar air heaters (SAH) provide an eco-friendly and sustainable means of harnessing solar energy for various applications, promoting energy conservation, and mitigating the release of greenhouse gases. Their simplicity and adaptability make them valuable tools across different sectors, such as space heating [5-7], desalination [8], drying of agricultural and industrial products [9,10], etc. However, the main drawback of SAHs operating within moderate temperature ranges is their poor thermal efficiency [11,12]. In an effort to improve the thermal performance of SAHs as a whole,

http://doi.org/10.30684/etj.2024.145706.1660
Received 30 December 2023; Received in revised form 14 February 2024; Accepted 20 February 2024; Available online 31 March 2024
2412-0758/University of Technology-Iraq, Baghdad, Iraq

researchers have conducted exhaustive studies on a variety of techniques, all to develop more efficient collectors, such as αρτιφιχιαλ surface roughness [13-15], employing phase change material [16,17], coating absorber plates [18], and extended surfaces [19-21]. Among the several strategies for improving SAH performance, one extremely successful strategy for improving heat transmission involves including porous materials, particularly metal foams, into the channels [22]. When using porous material, the thermal performance factor is higher than solar air heaters with turbulators of various geometries [23]. The porous systems' increased thermal and thermo-hydraulic efficiency may be ascribed to the more uniform temperature distribution and improved fluid mixing. In addition to its excellent efficiency, the porous layer does not create trapped vortices like traditional tabulators do, resulting in the absence of localized areas of high temperature (hot spots).

The incorporation of porous substrates into the collector channel has been the subject of an abundance of literature. Chen et al. [24] analyzed the energy storage process within a solar flat-plate collector that incorporated paraffin-filled aluminum foam. The results suggest modeling the PCM in porous foam using non-thermal rather than thermal equilibrium. Furthermore, utilizing aluminum foam loaded with paraffin resulted in a substantial enhancement in heat transfer efficiency. Rashidi et al. [25] did a sensitivity analysis to assess the influence of the Darcy number (Da). Reynolds number (Re), and thickness of the porous substrate (Hf) on combined convection-radiation heat transfer in a heat exchanger loaded with a porous medium of varied thicknesses. The investigation indicated that Re affects pressure drop and Nu is less for high Da and porous medium thickness. At greater thicknesses, the Nu is extremely sensitive to variations in porous substrate thickness. Bovand et al. [26] disclosed that the adoption of a porous substrate into the SAH results in a significant increase in the Nu. In particular, at $Da = 10^{-2}$ the aforementioned enhancements can be realized at multipliers of 3, 4.4, and 5.9 when the porous layer thickness is 1/3, 2/3, and 1, respectively. Furthermore, an augmentation in the Da and a reduction in the thickness of the porous layer are correlated with a corresponding escalation in the pressure drop within the system. A perturbation solution was presented in the study of Jamal-Abad et al. [27] to analyze convection-radiation heat transmission within a porous medium-filled SAH. According to their findings, as the shape parameter of the porous media increases, the Nu and pressure loss both increase. The shape parameter informs how porous and permeable the porous layer is. Jouybari et al. [28] discovered that adding a porous substrate to a flat plate solar collector (FPSC) resulted in an 82% increase in the Nu. They stated that using porous foam improves optical efficiency and decreases heat losses, particularly at lower Re. Nevertheless, attaining this enhancement necessitates greater pumping power due to an escalation in pressure loss throughout the channel. The highest overall performance parameter of 0.21 was achieved.

The thermal features of an FPSC channel featuring a partially or completely filled porous substrate were examined by Saedodin et al. [29]. Their findings suggested that the LTE assumption is appropriate for forecasting the thermal efficiency of FPSC with porous material. Furthermore, the research emphasized the possibility of achieving substantial enhancements in thermal efficiency and the Nu by 18.5% and 82%, respectively, through the utilization of this particular arrangement. Another experimental work by Jouybari et al. [30], examined the thermal performance of FPSC that uses nanofluid (SiO_2/deionized water) flow through a metal porous foam channel. They showed that nanofluid increases thermal efficiency by 8.1%. However, adding porous medium and nanofluid increases pressure drop, which should be considered in system design. The same team also analyzed heat transmission in a porous FPSC channel [31]. The results of their study indicated that the shape parameter of the porous material substantially impacts Nu and thermal performance within the FPSC channel. However, evaluating these parameters requires a careful balance between pressure drop and heat transfer considerations to provide a comprehensive assessment. Valizade et al. [32] conducted an experimental study that examined the impact of incorporating copper metal foam in a direct absorption parabolic trough solar collector. They showed that thermal efficiency was enhanced by up to 171% for completely permeable collectors and a rise of up to 119% for partly filled collectors. In contrast, the porous solar collector exhibited a significant increase in the friction factor, surpassing values in the empty collector by up to two orders of magnitude. According to Jouybari and Lundström [23], adding a thin porous layer on the absorber plate significantly influences the SAH's thermal and thermo-hydraulic performance. This improvement is substantial, with the highest surpassing 5 times when compared to an SAH lacking a porous medium. Anirudh and Dhinakaran [33] performed a numerical analysis to improve the thermal performance of an FPSC by inserting porous metal foam blocks. Their findings show that as the number of porous blocks grows, so does heat transmission and pressure drop. Surprisingly, the study discovered that the best thermo-hydraulic performance of around 1.9 was obtained with the fewest blocks of the smallest thickness, especially at high Da. In another numerical study, Anirudh and Dhinakaran [34] showed that the thermal characteristics of the FPSC channel benefit from employing a conjugated arrangement of porous bodies; this method improves heat transfer by promoting thermal mixing and redirecting a larger amount of the flow to the higher absorber plate. Keeping the block's height low near the inlet and high near the outflow produced the best performance factor of 2.163. A numerical investigation was carried out by Diganjit et al. [35] to improve heat transmission by utilizing discrete metal foam blocks with varying thickness and porosity in SAH. The Nu improved by 157.64% to 218.60% compared to the empty channel. Thus, they concluded that metal foam has the potential to serve as a highly effective choice for improving heat transmission in a SAH, provided that it undergoes appropriate design considerations. To explore heat transfer enhancement, turbulent flow in a heated square channel with solid or metal foam baffles of 95% copper porosity was tested by Fadhala et al. [36]. They staggered the baffles with a gradient pore density on the top and bottom walls. Results showed that baffles with a gradient pore density of 10/20 PPI had better thermo-hydraulic performance than all copper foam baffle models. A chamfered structural design within a porous cavity was recently proposed and tested by Fu et al. [37] to enhance the thermal performance of FPSC by reducing fluid flow resistance. The author showed that incorporating this cavity structure increases the global Nu, decreases the friction factor, and improves PEC. The PEC demonstrates a peak increase of 12.5% compared to designs lacking the chamfered structure. Xia et al. [1,38] conducted a numerical analysis to examine the

comprehensive heat transfer characteristics within the FPSC channel. This study considered different shapes of porous blocks, quantity, permeability, and materials that were inserted into the FPSC channel. They showed that using rectangular porous blocks clearly enhances heat transport within the FPSC channel. The optimal performance factor of 1.8 was achieved when the number of blocks was adjusted to 6, especially in situations with high permeability $Da = 10^{-2}$. However, it is important to note that the friction factor reached its maximum value when N was set to 4. Table 1 below summarized some numerical studies conducted on porous assisted solar systems.

From examining existing literature, the authors identified a notable gap in understanding the influence of metal foam on solar air heater (SAH) performance. Moreover, despite the abundance of research on metal foams, there is a lack of attention to the impact of pore density, permeability, and metal foam thickness on SAH performance. Accordingly, this paper focuses on the numerical simulation of a SAH system partially or completely filled with copper metal foam utilizing the commercial software ANSYS FLUENT 2023 R1, assuming local thermal non-equilibrium. The simulations were carried out for various pore densities (ω=10-40 PPI), Reynolds number (Re=6000-16000), and different dimensionless foam heights (H_f=0-1) to achieve an ideal foam height that simultaneously enhances heat transmission and minimizes pressure loss. Finally, a comprehensive analysis of the thermo-hydraulic performance factor (TPF) was conducted to identify the optimal trade-off between enhanced heat transfer and pressure drop in the Solar Air Heater (SAH) channel. This examination aims to determine the conditions that yield the highest TPF value. The outcomes of this study can serve as valuable technical evidence, providing insights for potential future applications of SAH systems utilizing porous materials in both residential and commercial contexts.

2. Problem description and assumptions

Figure 1a depicts the geometry of the solar air heater under consideration in this work. The solar air heater duct has a cross-section of 300 mm × 25 mm. It consists of three sections: the entrance portion is 525 mm long, the test section is 1000 mm long, and the exit section is 875 mm long. These dimensions are in accordance with the requirements set by ASHRAE Standard 93 [39]. Before entering the testing region, the fluid must achieve hydro-dynamically fully developed flow. The entrance part's purpose is to ensure this condition's attainment. On the other hand, the exit section mitigates the impact of departure disturbances or disruptions in the test section.

Figure 1b illustrates the arrangement where the absorber plate is surrounded by a copper metal foam substrate with a height (h_f) that can be changed. This design yields metal foam structures of different dimensionless heights (H_f) ranging from 0 (representing an empty channel) to 1 (showing a completely filled channel).

It is assumed that the heat flux along the absorber plate is uniform. Both the top and lower channel walls are insulated. The air flows into the channel at a constant temperature and velocity. The flow is considered two-dimensional, steady, incompressible, and turbulent. Moreover, it is important to mention that the foam matrix is treated as isotropic, and it is assumed that the thermo-physical properties of both the fluid and the solid remain constant, as detailed in Table 2. The flow is modeled using the Darcy extended Forchheimer (DEF) equations in a porous matrix to account for viscous and inertial effects. The two-equation temperature model (LTNE) provides the basis for the mathematical explanation of energy transfer, where the temperatures of the solid and fluid are independently solved [40,41].

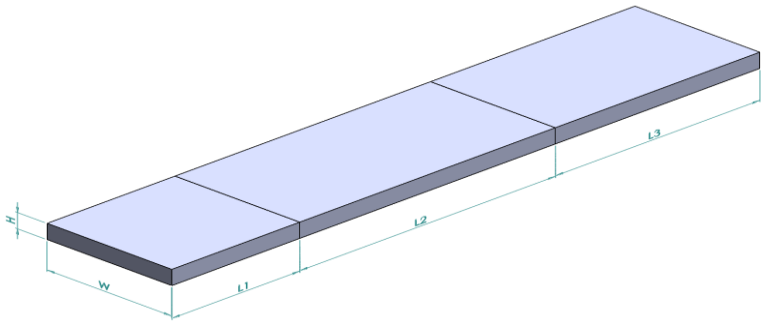

(a)

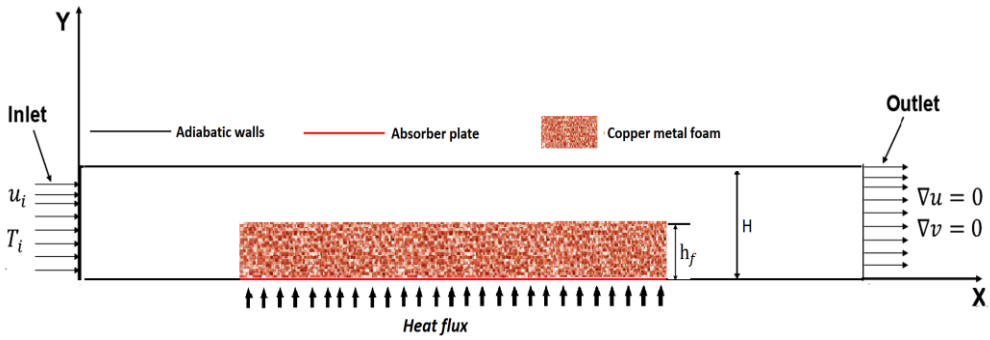

(b)

Figure 1: Schematic of foam-assisted SAH, (a) 3D view (b) computational domain

Table 1: Summary of numerical studies conducted on porous assisted solar systems

Models used	Contributions	Key Features Introduced	Ref.
Darcy - extended Forchheimer model, with LTE model. The effect of turbulence within the porous medium is modeled with a macroscopic k-ε model	The effects of covering the absorber plate of a solar air heater with a thin porous material, considering the turbulence impact within the porous layer	A thin, porous layer improves thermal performance compared to solar air heaters with different turbulators. The recommended configuration prevents trapped eddies above the absorber plate, reducing hot spots	[23]
Brinkman-Forchheimer extended the Darcy model with the LTNE model	Examination of the impact of metal foam loaded with paraffin on a solar flat-plate collector performance	The phase-change heat transfer mechanism in the solar collector may be better predicted by assuming LTNE between metal foams and paraffin, which is closer to the real-world situation	[24]
Brinkman-Forchheimer extended the Darcy model with the LTE model	The impact of various factors on the convection-radiation heat transfer and flow structures within a solar heater	Adopting porous substrate into SAH significantly increases the Nusselt number (Nu)	[26]
Brinkman-Forchheimer extended Darcy model The heat transfer equation has been solved analytically based on the perturbation method	Temperature-dependent radiative conductivity was used to evaluate the performance of a porous channel solar collector	Radiation has a more significant impact on collector thermal performance and the Nu than the porous shape parameter	[31]
Brinkman-Forchheimer extended the Darcy model with the LTE model	The influence of porous blocks' height, number, permeability, and arrangement were studied	For the porous channel, it is confirmed that the extended Darcy-Brinkman-Forchheimer model is the right choice Optimal performance is attained when the inlet and outflow are free of porous blocks	[33]
Brinkman-Forchheimer extended the Darcy model with the LTE model	The thermal characteristics of conjugated porous blocks within FPSC were investigated	The highest performance is observed when the height of the block is lower near the inlet and higher near the outflow	[34]
Darcy - extended Forchheimer model, with LTNE model	Utilization of discrete metal foam blocks with varying thickness and porosity in SAH	Employing a discrete arrangement of metal foam reduces pressure drop while maintaining effective heat transmission	[35]
Brinkman-Forchheimer extended the Darcy model with the LTE model	Present an innovative design for enhancing the thermal performance of a flat-plate solar collector (FPSC) via porous media	The chamfered cavity structure leads to an increase in the global Nu and a reduction in the friction factor, resulting in an improved PEC value	[37]
Brinkman-Forchheimer extended the Darcy model with the LTE model	This study examined different designs of porous blocks, their amount, permeability, and the materials used when they were introduced into the FPSC channel.	Using a large number of rectangular porous blocks with high permeability enhances heat transfer efficiency within the FPSC channel	[1, 38]
Darcy - extended Forchheimer model, with LTNE model	Simulations focused on fluid flow and heat transfer within an SAH channel incorporating copper metal foam with a porosity of 90% were carried out		Present

Table 2: Thermo-physical properties in this study

Properties	Unit	Porous media (Cu)	Air (Pr=0.741)
$\boldsymbol{\rho}$	kg/m^3	8978	1.225
$\boldsymbol{c_P}$	$J/kg.K$	381	1006.43
$\boldsymbol{\lambda}$	$W/m.K$	387.6	0.0242
$\boldsymbol{\mu}$	$kg/m.s$	---	1.7894×10^{-5}

The average hydraulic diameter based Re number and average Nu number can be defined as in Equations (1 and 2) respectively [23]:

$$Re = \frac{\rho\, u_{av} D_h}{\mu_f} \tag{1}$$

$$Nu = \frac{\bar{h}\, D_h}{\lambda_f} \tag{2}$$

where $\bar{h}$ is the average heat transfer coefficient, which can be derived from the following expression [23]:

$$h_x = \frac{\acute{q}}{T_w - T_{m,x}}, \qquad \bar{h} = \frac{1}{L_2} \int_{x=L_1}^{x=L_2} h_x \; dx \tag{3}$$

where $T_{m,x}$ represents the mean temperature of the fluid in the cross-section at position *x*. This mean temperature is expressed as follows [23]:

$$T_{m,x} = \frac{1}{H\, u_{m,x}} \int_{y=0}^{y=H} u\, T\, dy \tag{4}$$

The term $u_{m,x}$ denotes the mean velocity at the identical cross-section, which can be expressed as [23]:

$$u_{m,x} = \frac{1}{H} \int_{y=0}^{y=H} u \; dy \tag{5}$$

The Fanning friction factor, f, is defined as [42]:

$$f = \frac{\Delta P}{2\rho u^2} . \frac{D_h}{L} \tag{6}$$

The Nu and f for an empty channel are determined using the Dittus- Boelter and modified Blasius equations, Equations (7 and 8) respectively, as specified in [43].

$$Nu_s = 0.023 Re^{0.8} Pr^{0.4} \tag{7}$$

$$f_s = 0.085 Re^{-0.25} \tag{8}$$

Webb and Eckert [44] introduced a metric to assess the heat transfer efficiency of a modified duct, like those featuring roughened surfaces, relative to a smooth duct while maintaining constant pumping power. This performance metric is called the thermo-hydraulic performance factor (TPF), in Equation (9):

$$TPF = \frac{{}^{Nu}/_{Nu_s}}{\left({}^{f}/_{f_s}\right)^{1/3}} \tag{9}$$

The Thermo-hydraulic Performance Factor (TPF) is utilized to quantitatively assess the simultaneous influence of incorporating a porous material into the SAH on both the heat transmission enhancement and pressure drop penalty.

3. Numerical formulations

3.1 Numerical simulation methods

The simulations used the commercial ANSYS FLUENT software, specifically version 2023 R1, employing the FVM approach while considering the required boundary conditions. For this investigation, the $k-\varepsilon$ viscous model in ANSYS Fluent was employed. The simulations utilized a planar-space steady-state pressure-based solver with double precision. The discretization of convection and diffusion terms was discretized using a Green-Gauss node-based approach. The momentum, energy, and turbulence equations were spatially discretized using a second-order upwind scheme, and a second-order scheme was applied for the space discretization of pressure. The SIMPLE algorithm managed the interplay between the pressure and velocity domains. The convergence criteria were established using residuals to guarantee the accuracy of the solution. For the continuity and momentum equations, a residual limit of 10^{-4} was employed in this study, whereas an even more rigorous limit of 10^{-6} was applied to the energy equation.

3.2 Governing and turbulent equations

The fluid flows through the unoccupied space and channel sections containing metallic foam. In the case of turbulent airflow within the channel's open space, a standard $k-\varepsilon$ turbulence model is employed, as reported in [45,46]. The following are the governing equations evaluated in accordance with the assumptions stated above [47,48]:

- Governing equations for the fluid zone (turbulent flow) :

Continuity equation:

$$\frac{\partial(\rho_f u_i)}{\partial x_i} = 0 \tag{10}$$

Momentum equation:

$$\frac{\partial(\rho_f u_i u_j)}{\partial x_i} = -\frac{\partial p}{\partial x_i} + \frac{\partial}{\partial x_j}\left[(\mu_f + \mu_t)\left(\frac{\partial u_i}{\partial x_j} + \frac{\partial u_j}{\partial x_i}\right)\right] \tag{11}$$

Energy equation:

$$\frac{\partial}{\partial x_i}(\rho_f u_i \mathrm{T}) = \frac{\partial}{\partial x_j}\left[\left(\frac{\mu_f}{Pr_f} + \frac{\mu_t}{Pr_t}\right)\frac{\partial T}{\partial x_j}\right] \tag{12}$$

The turbulent kinetic energy (k) and rate of energy dissipation (ε) are expressed as follows in equations 13 and 14, respectively [47,48]:

$$\overline{u_J}\frac{\partial k}{\partial x_j} = \mu_t\left[\left(\frac{\partial \overline{u_i}}{\partial x_j} + \frac{\partial \overline{u_J}}{\partial x_i}\right)\frac{\partial \overline{u_i}}{\partial x_j}\right] - \mathcal{E}\frac{\partial}{\partial x_j}\left[\left(\mu + \frac{\mu_t}{\sigma_k}\right)\frac{\partial k}{\partial x_j}\right] \tag{13}$$

$$\overline{u_J}\frac{\partial \varepsilon}{\partial x_j} = C_{\mathcal{E}1}\,\mu_t\frac{\mathcal{E}}{k}\left[\left(\frac{\partial \overline{u_i}}{\partial x_j} + \frac{\partial \overline{u_J}}{\partial x_i}\right)\frac{\partial \overline{u_i}}{\partial x_j}\right] - C_{\mathcal{E}2}\,\frac{\mathcal{E}^2}{k} + \frac{\partial}{\partial x_j}\left[\left(\mu + \frac{\mu_t}{\sigma_\epsilon}\right)\frac{\partial \varepsilon}{\partial x_j}\right] \tag{14}$$

Where

$$\mu_t = \rho C_\mu \frac{k^2}{\mathcal{E}} \tag{15}$$

The μ_t denotes the turbulent viscosity while σ_k and σ_ϵ are constants known as turbulent Prandtl numbers associated with k and ε. The values assigned to these turbulent model constants in the above equations align with those previously reported [47,48]:

$C_{\mathcal{E}1} = 1.44, \quad C_{\mathcal{E}2} = 1.92, \quad C_\mu = 0.09, \quad \sigma_k = 1.0, \quad \sigma_\epsilon = 1.$

- Governing equations for foam zone [47,48]:
- Continuity equation:

$$\frac{\partial(\rho_f \emptyset\, u_i)}{\partial x_i} = 0 \tag{16}$$

Momentum equation (Darcy-Extended Forchheimer model):

$$\frac{\partial(\rho_f u_i u_j)}{\partial x_i} = -\emptyset\frac{\partial p}{\partial x_i} + \frac{\partial}{\partial x_j}\left[\mu_f\left(\frac{\partial u_i}{\partial x_j} + \frac{\partial u_j}{\partial x_i}\right)\right] - \emptyset\left(\frac{\mu_e}{K}\,u_i + \frac{\rho_f C_F}{\sqrt{K}}\,|u|u_i\right) \tag{17}$$

Energy equations for local thermal non-equilibrium model.

- For fluid [46]:

$$\emptyset\frac{\partial}{\partial x_j}(\rho_f c_{p,f}\,u_j \mathrm{T}_f) = \lambda_{fe}\,\frac{\partial}{\partial x_j}\left(\frac{\partial \mathrm{T}_f}{\partial x_j}\right) + h_{sf}\,a_{sf}\,(\mathrm{T}_s - \mathrm{T}_f) \tag{18}$$

- For solid [46]:

$$0 = \lambda_{se}\,\frac{\partial}{\partial x_j}\left(\frac{\partial \mathrm{T}_s}{\partial x_j}\right) - h_{sf}\,a_{sf}\,(\mathrm{T}_s - \mathrm{T}_f) \tag{19}$$

In the above, K, λ_{se}, λ_{fe}, a_{sf} , and h_{sf} are unique characteristics specific to metallic foams and can be obtained or derived from the information provided in Table 3.

Considering that the two sets of governing equations are linked at the interface between the porous and fluid phases, defining the interfacial coupling conditions is crucial to conclude Equations appropriately. 10-19. To uphold meaningful physics, it is necessary to ensure the continuity of velocity, shear stress, fluid temperature, and heat flux at the porous-fluid interface. The corresponding expressions are denoted by Equations (20–24) [46].

$$u|_{y_i^-} = u|_{y_i^+} \tag{20}$$

$$\frac{\mu_f}{\emptyset}\frac{\partial u}{\partial y}\Big|_{y_i^-} = \mu_f \frac{\partial u}{\partial y}\Big|_{y_i^+} \tag{21}$$

$$T_f\big|_{y_i^-} = T_f\big|_{y_i^+} \tag{22}$$

$$\lambda_{se}\ \frac{\partial T_s}{\partial y} + \lambda_{fe}\ \frac{\partial T_f}{\partial y}\Big|_{y_i^-} = \lambda_f\ \frac{\partial T_f}{\partial y}\Big|_{y_i^+} \tag{23}$$

$$-\lambda_{se}\ \frac{\partial T_s}{\partial y}\Big|_{y_i^+} = h_{sf}\ (T_s|_{y_i^+} - T_f\big|_{y_i^-}) \tag{24}$$

3.3 Boundary conditions

The following are the boundary conditions that can be specified for an SAH channel partially filled with metallic foams:

(1) At inlet ($x = 0, \quad 0 \le y \le H$), the steady flow with a uniform fluid velocity and temperature is given:

$$u = U_o, \quad v = 0, \qquad T = T_o$$

(2) At exit ($x = L_1 + L_2 + L_3, \quad 0 \le y \le H$), the fully developed conditions are fulfilled:

$$\frac{\partial u}{\partial x} = 0, \qquad \frac{\partial v}{\partial x} = 0, \qquad \frac{\partial T}{\partial x} = 0$$

(3) Along the upper walls ($0 \le x \le L_1 + L_2 + L_3, y = H$), the no-slip conditions and the perfect-insulated plates are taken:

$$u = 0, \quad v = 0, \qquad \frac{\partial T}{\partial y} = 0$$

(4) Along the lower walls ($0 \le x \le L_1 + L_2 + L_3, y = 0$), the no-slip conditions are taken.

$$u = 0, \quad v = 0$$

at insulation area ($0 \le x \le L_1, \quad L_1 + L_2 \le x \le L_1 + L_2 + L_3, \quad y = 0$):

$$\frac{\partial T}{\partial y} = 0$$

at heat sources area in absorber plate ($L_1 \le x \le L_1 + L_2, \quad y = 0$) (porous region):

$$\acute{q} = -\lambda_{se}\ \frac{\partial T_s}{\partial y} - \lambda_{fe}\ \frac{\partial T_f}{\partial y}, \qquad T_f = T_s = T_w$$

3.4 Grid study

To enhance the quality of the solution, a finite number of rectangular/quad cells are utilized to discretize the two-dimensional computational model. The grid has been refined near the wall between the fluid layer and the porous medium. Figure 2 illustrates the generated geometry, which has been elongated along the axial to enhance visibility. To verify the accuracy of the numerical solutions, a grid independence test was performed using five sets of grid systems in simulations at $H_f = 0.6$, $\omega = 10PPI$, and $Re = 10{,}000$. Table 4 shows a discrepancy of around 0.043% in the Nu between the two sets of computed values for grids with 525,232 and 417,389 elements, respectively. Consequently, the grid with 525,232 cells has been chosen for the remaining simulations

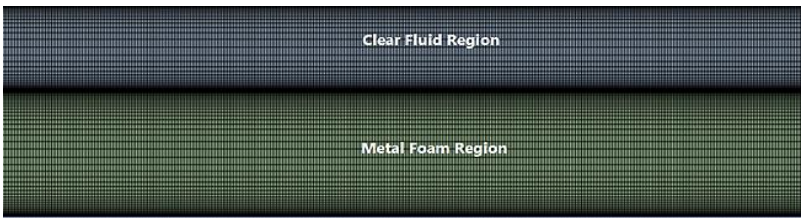

Figure 2: Distribution of grids within the computational domain for the case of H_f=0.6

Table 3: Correlations for metallic foams' parameters

Parameter	Correlation	Ref.
Pore diameter (d_p)	$d_p = \frac{0.0254}{\omega}$	[49]
Fiber diameter (d_f)	$\frac{d_f}{d_p} = 1.18\sqrt{\frac{(1-\phi)}{3\pi}}\frac{1}{1-e^{-(1-\phi)/0.04}}$	[49]
Permeability (K)	$K = 0.00073 d_p^2 (1-\phi)^{-0.224}\left(\frac{d_f}{d_p}\right)^{-1.11}$	[49]
Specific surface area (a_{sf})	$a_{sf} = \frac{3\pi d_f}{(0.59 d_p)^2}\left[1-e^{-(1-\phi)/0.04}\right]$	[50]
Local heat transfer coefficient (h_{sf})	$Nu_{sf} = \frac{h_{sf} d}{k_f} = \begin{cases} 0.76\mathrm{Re}_d^{0.4}\,\mathrm{Pr}^{0.37}, (1 \le \mathrm{Re}_d \le 40) \\ 0.52\mathrm{Re}_d^{0.5}\,\mathrm{Pr}^{0.37}, (40 \le \mathrm{Re}_d \le 10^3) \\ 0.26\mathrm{Re}_d^{0.6}\,\mathrm{Pr}^{0.37}, (10^3 \le \mathrm{Re}_d \le 2\times10^5) \end{cases}$ $d = \left(1-e^{-(1-\phi)/0.04}\right)d_f$ $\mathrm{Re}_d = \frac{\rho_f u d}{\mu_f}$	[50]
Effective thermal conductivity (λ_e)	$\lambda_e = \frac{1}{\sqrt{2}(R_A + R_B + R_C + R_D)}$ Where, $R_A = \frac{4\lambda}{(2e^2 + \pi\lambda(1-e))\lambda_s + (4 - 2e^2 - \pi\lambda(1-e))\lambda_f}$ $R_B = \frac{(e-2\lambda)^2}{(e-2\lambda)e^2\lambda_s + (2e - 4\lambda - (e-2\lambda)e^2)\lambda_f}$ $R_C = \frac{(\sqrt{2}-2e)^2}{2\pi\lambda^2(1-2\sqrt{2}e)\lambda_s + 2(\sqrt{2} - 2e - \pi\lambda^2(1-2\sqrt{2}e))\lambda_f}$ $R_D = \frac{2e}{e^2\,\lambda_s + (4-e^2)\lambda_f}$ $\lambda = \frac{\sqrt{\sqrt{2}(2-(5/8)e^3\sqrt{2}-2\phi)}}{\pi(3-4\sqrt{2}\,e-e)}$, $e = 0.339$ Then, $\lambda_{fe} = \lambda_e \; at \; \lambda_s = 0$, and $\lambda_{se} = \lambda_e \; at \; \lambda_f = 0$	[51]

Table 4: Impact of grid size on Nu for $H_f = 0.6$, $\omega = 10PPI$, and $Re = 10{,}000$

No.	No. of Elements	Nu	Percentage Difference
1	240,000	346.858	1.829%
2	285,385	340.513	1.840%
3	342,829	334.249	1.787%
4	417,389	328.275	0.003%
5	525,232	328.265	-----

3.5 Validation procedure

3.5.1 Clear flow region

The Nu and f values for the smooth duct, obtained by the present numerical approach, were compared to those calculated using the empirical correlations (Equations 7 and 8), respectively. Additionally, the current results were compared to the

experimental findings of Patel et al. [43], as shown in Figure 3a and b for Nu and friction factor respectively. The pattern similarity between the Nu and f plots is evident. The maximal divergence from the empirical correlation for Nu was found to be 6%, while the variations compared to experimental data were found to be within the range of 1.28 to 8.4%. Similarly, for the friction factor (f), deviations ranged from 6.1 to 8.7% and from 0.19 to 3.38%, respectively. Based on this comparison, it may be inferred that the existing numerical technique yields satisfactory outcomes.

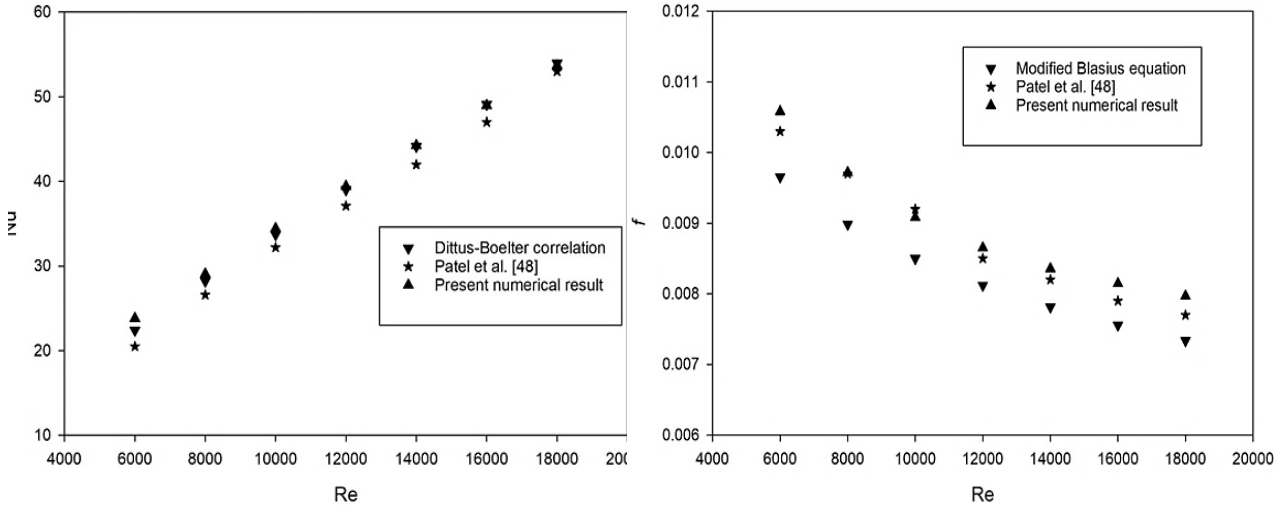

(a) (b)

Figure 3: Comparison of the current numerical findings with the experimental data obtained [43] and empirical correlation for (a) Nu, and (b) friction factor

3.5.2 Porous region

The experiment conducted by Dukhan et al. [52] was simulated for validation, and the predicted results were compared to the current study's findings. The experimental setup involved a fully filled, heated open-cell aluminum foam cylinder with a constant heat flux at the wall, cooled by water flow with an inlet velocity of 0.0049 m/s. The inside surface of the tube was lined with 87.6% porosity aluminum foam. The plots in Figure 4 present the experimental and numerical results for wall temperature at various axial distances. The fact that the numerical calculations' results match the experimental trends indicates that the two sets of results are in good agreement.

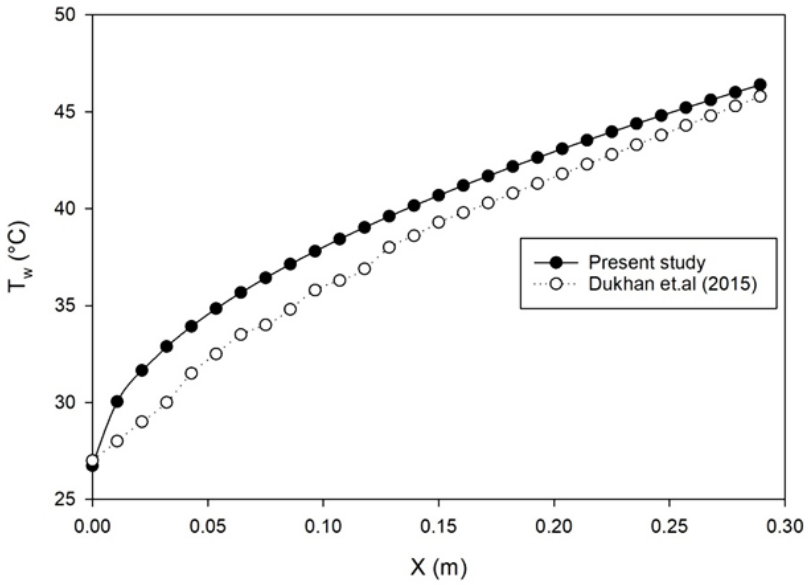

Figure 4: Comparison of the current numerical findings with the experimental data of Dukhan et al.[52] for wall temperature along the axial distance

The current model was also verified using the outcomes of Saedodin et al. [29] for an FPSC filled with copper metal foam at various flow rates. The metal foam has a porosity of 0.93 and a pore density of 20 PPI. The comparisons in Figure 5a and b indicate that the average Nu and f are in good agreement with their numerical and experimental values. The friction factor and

the average Nu exhibit maximal relative deviations of 3.13% and 4.57%, respectively. Therefore, the anticipated outcomes justify the utilization of the aforementioned numerical model in the subsequent investigation.

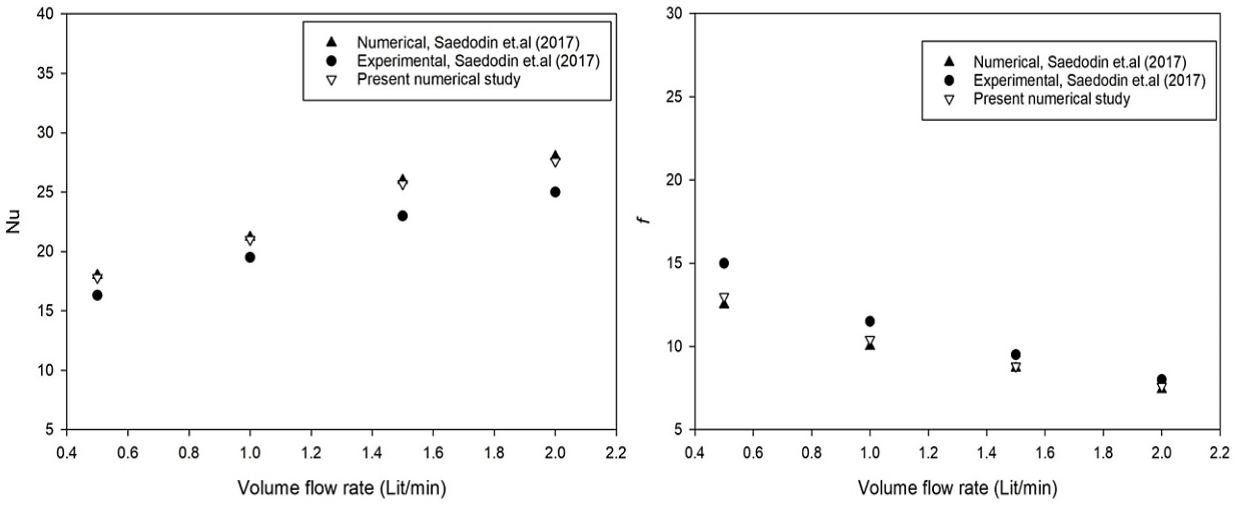

(a) (b)

Figure 5: *Co*mparison between the present numerical results and the result of Saedodin et al. [29] for (a) Nu, and (b) friction factor

4. Results and discussion

4.1 Velocity profiles

4.1.1 The effect of foam height

The velocity contours inside the heater for different foam heights and Re = 16000 are shown in Figure 6. According to the Figure, the velocity within the porous substrate is much lower than that in the clear fluid zone for the partially filled channel ($H_f = 0.2 - 0.8$). The high resistance shown by the porous substrate causes this difference in velocity. Furthermore, the velocity exhibits an upward trend with the dimensionless foam height in the fluid zone. This phenomenon occurs because increasing dimensionless foam height decreases the cross-sectional area in the fluid zone. As a result, the clear fluid zone experiences a higher velocity.

The influence of several critical variables on the velocity profile is evident in Figure 7 (a–c). The impact of dimensionless foam height ($H_f = 0, 0.2, 0.4, 0.6, 0.8 \; and \; 1$) on the velocity profile at a location $x = L_1 + L_2/2$ is depicted in Figure 7a. The velocity profile of a filled channel ($H_f = 1$) is identical to that of a smooth channel ($H_f = 0$), except for a more uniform distribution due to the absence of an abrupt change in permeability across the cross-section. The velocity in the foam zone of the partially filled metallic foam channel has a homogenous characteristic. The sudden increase in permeability at the interface between the porous material and the fluid causes a rapid change in the velocity distribution at that contact, leading to a maximum velocity in the fluid zone. The statement suggests an upward relationship exists between the height of the metal foam substrate and the peak velocity, meaning that as the height grows, the peak velocity also increases. This phenomenon is ascribed to the heightened fluid flow within the fluid zone. The reduced height of the fluid region, linked to the increased thickness of the metallic foam, enables more effective and focused fluid motion. Consequently, the peak velocity, which refers to the highest speed of the fluid flow, tends to rise. The significantly lower velocity in the foam region suggests that most of the fluid passed through the open region, with just a small amount passing through the foam region.

4.1.2 The effect of Re

Figure 7b shows the velocity profiles under different Re numbers when $h_f = 15\,mm$ ($H_f = 0.6$). It is discovered that when the Re number grows, the fluid velocities within partially filled channels (both the foam area and the fluid region) all increase, where higher Reynolds numbers frequently equate to more energetic and faster-flowing fluid. Additionally, it is worth noting that the velocities of the partially filled channel exhibit their maximum values at $H = 20\,mm$ when subjected to various Re numbers. The findings also demonstrate that the average velocity in the open zone is markedly greater than in the foam region. This indicates that, although there is a significant incoming flow velocity, the velocity within the foam zone is quite small.

4.1.3 The effect of pore density

The impact of pore density (ω) on the velocity profile is depicted in Figure 7c. Because the porous foam becomes less permeable as the pore density or porosity increases, an increase in pore density might slow down the flow in the foam zone and speed up the flow in the fluid zone. The increased flow resistance caused by the smaller holes in the 40 PPI foam leads to air

evading the foam area and moving away from higher PPI foam. Consequently, as the pore density grew, the fluid velocity decreased in the foam area and increased in the open area.

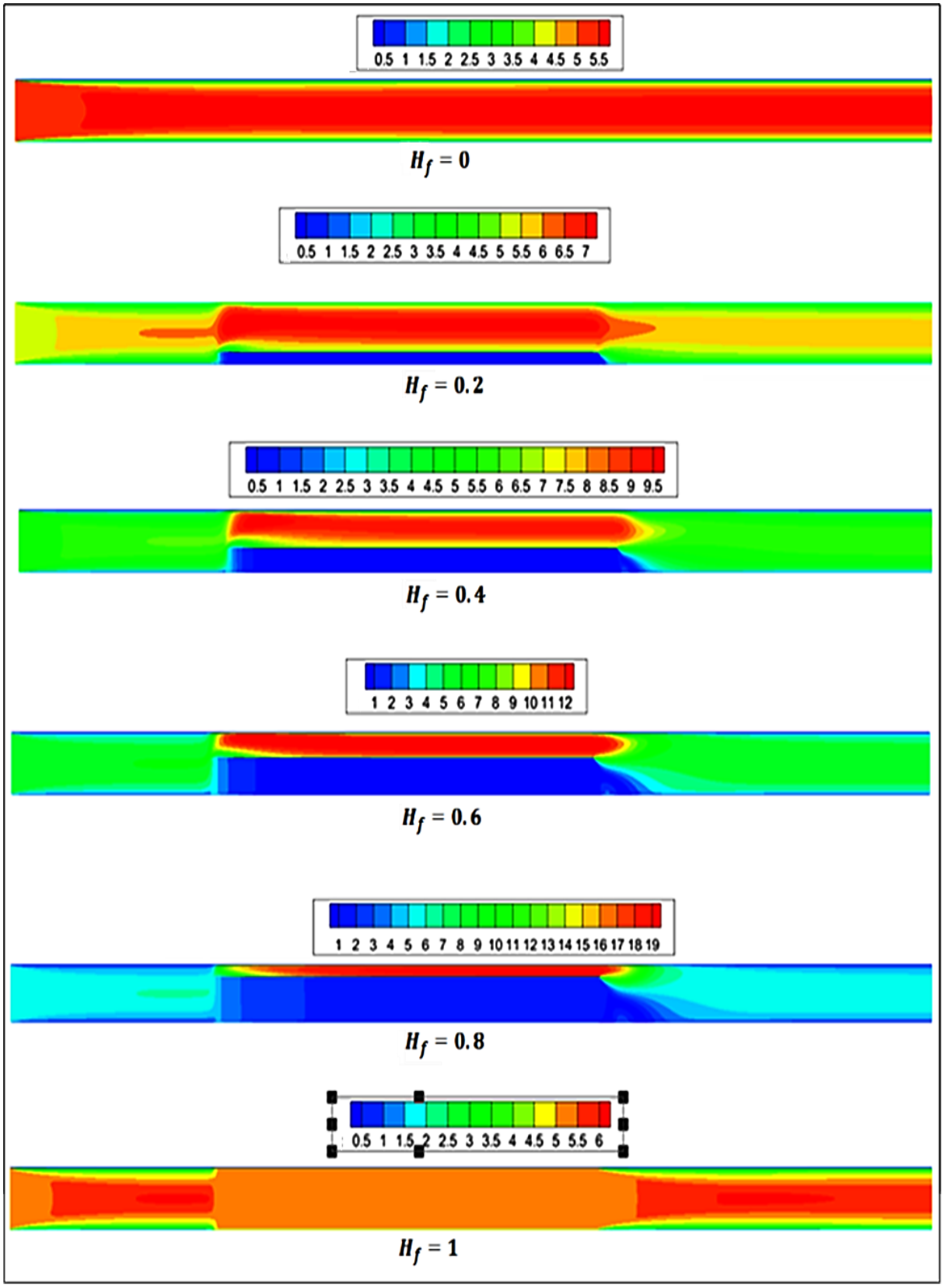

Figure 6: Velocity contours inside the heater at Re = 16000 for different dimensionless foam heights

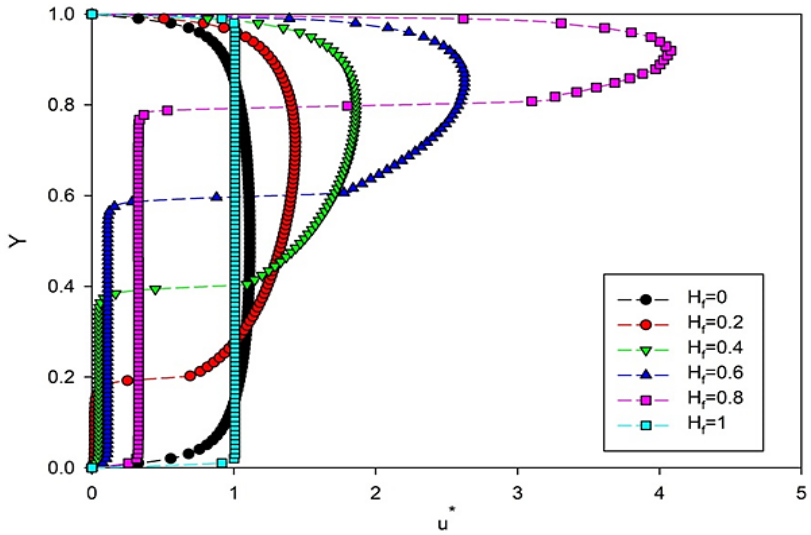

(a)

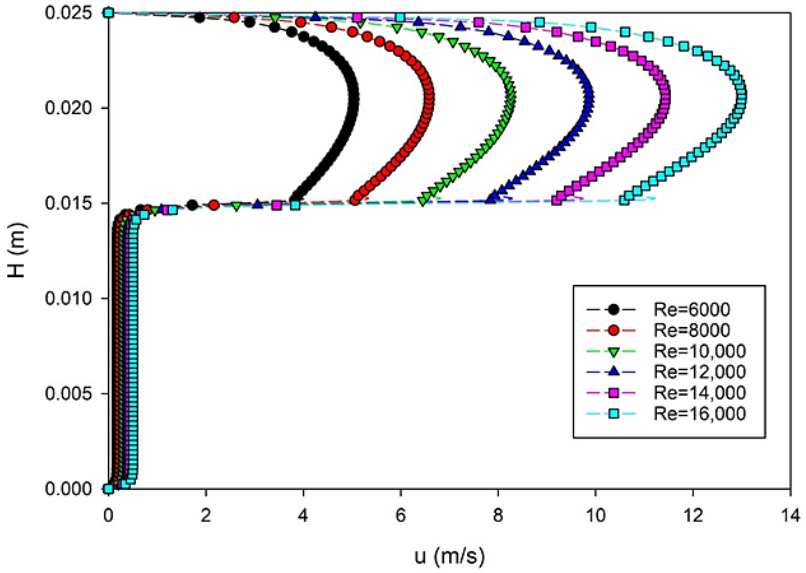

(b)

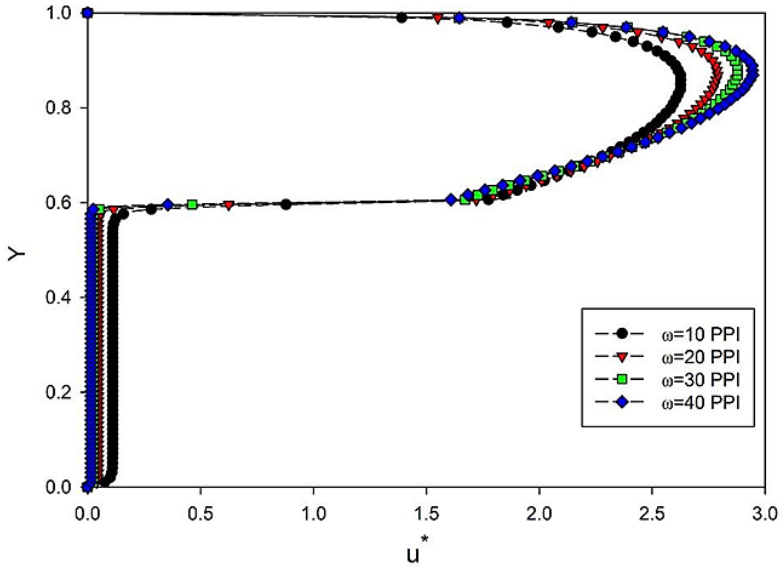

(c)

Figure 7: Impacts of key factors on velocity profile: (a) foam height (b) Re, and (c) pore density

4.2 Temperature distribution

4.2.1 Temperature contours

Figure 8 displays the temperature distribution patterns in relation to copper metal foam with a porosity of 0.9 and a pore density of 10 PPI. The temperature contours were plotted for various dimensionless foam heights at a Re 16000. Evidently, the highest temperature corresponds to the temperature in close proximity to the absorber plate. The absorber plate temperature is elevated for lower metal foam height, as seen in Figure 8. Also, the temperature distribution is nearly uniform throughout the channel, except near the absorber plate. As the thickness of the metal foam grows while maintaining the same PPI and porosity, the temperature of the absorber plate drops. This is because the increased thickness provides a larger surface for heat transmission. The contours exhibit greater irregularity when the heater is completely filled with porous material ($H_f = 1$). Considering the effect of heat conduction is crucial when including porous materials in the heater. Furthermore, using porous material has resulted in an amplified temperature differential along the wall.

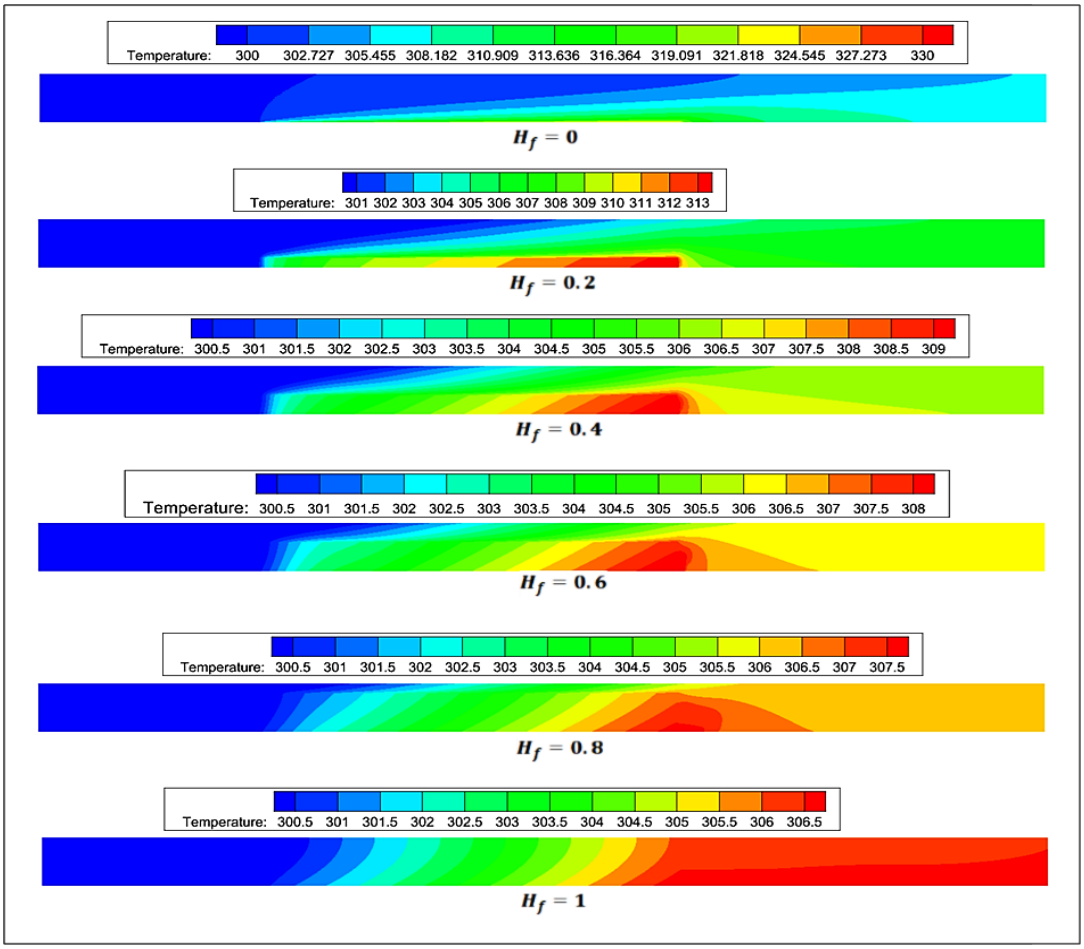

Figure 8: Temperature contours inside the heater at Re = 16000 for different dimensionless foam heights

4.2.2 Absorber plate temperature

The absorber plate temperatures computed in the current study for both the absorber with and without a metal foam layer covering it (empty) in the flow direction (x) at various foam heights, Re numbers, and pore densities are illustrated in Figure 9 (a-c). According to the Figures, the wall temperature tends to rise with increasing axial distance along the flow direction for a given heat flux. The observed behavior may be attributed to various factors, including convective heat transfer and heat conduction, which contribute to the rise in the fluid's temperature as it goes downstream.

According to Figure 9a, the plate temperatures with metal foams are consistently lower than those without, regardless of foam height. The improved heat transmission from the absorber plate can be due to three factors: i) the elevated thermal conductivity, ii) the increased fluid mixing within the porous medium, and iii) the higher surface area. A thinner boundary layer and a more homogeneous velocity profile result from these factors compared to an empty channel. The reduced plate temperature safeguards it against thermal stresses and breaking down when exposed to high temperatures [53]. Furthermore, the current configuration effectively eradicates hotspots by virtue of the porous media geometry that hinders eddies from forming on the plate. Therefore, it is recommended that foams with excellent conductivity be adhered to the duct's absorber wall.

Furthermore, the wall temperature decreases when the Reynolds number increases, as shown in Figure 9b. A higher Reynolds number indicates more fluid flows within the foam zone (higher velocity), enhancing convective heat transfer. This

enhancement of heat transmission tends to reduce the temperature of the wall. This trend is expected and very similar to what other experimental studies provide, such as Kurtbas and Celik [54] and Dukhan et al. [52,55]. The wall temperature is lower at higher flow velocities and foam heights, suggesting better heat transfer rates.

Figure 9c shows the absorber wall temperature for various pore densities at $Re = 16000$ and $H_f = 0.6$. As the permeability is enhanced by reducing the foam's pore density, the fluid traveling through the foam regains increases at low pore density values (high permeability). As the heater becomes more saturated with fluid, it carries away more heat, increasing convective heat transfer. This enhanced heat transfer tends to decrease the absorber wall temperature.

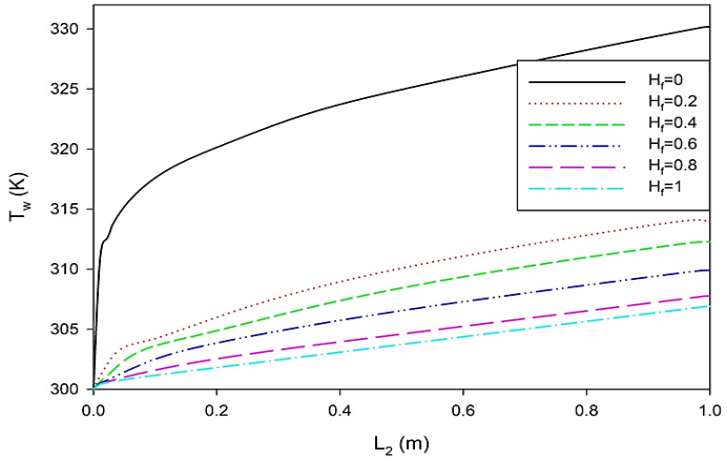

(a)

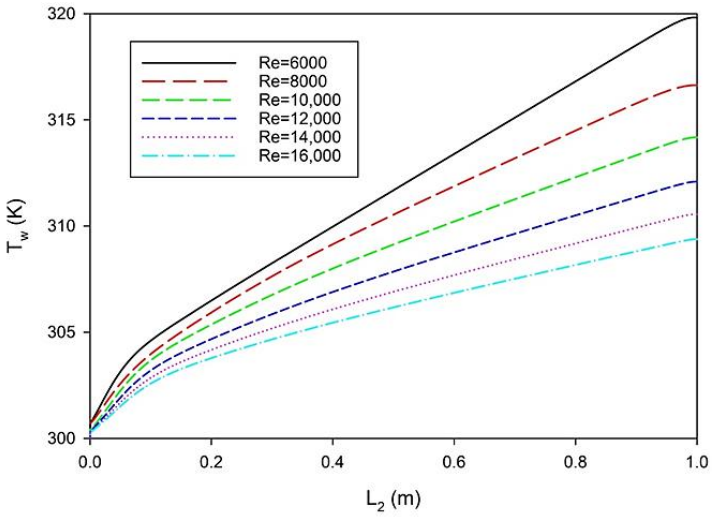

(b)

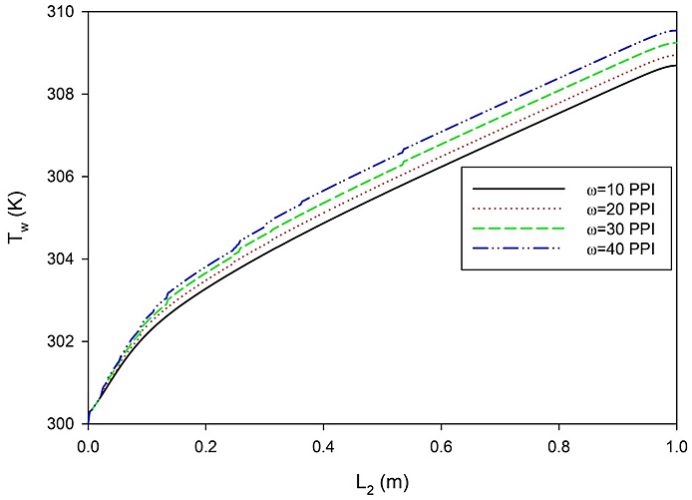

(c)

Figure 9: Impacts of key factors on absorber plate temperature: (a) foam height, (b) Re, and (c) pore density

4.2.3 Exit temperature

The temperature profiles across the height of the SAH duct at a specific distance $x = L_1 + L_2$ (test section exit) are shown in Figure 10a for various foam heights. The solar air heater with a metal foam layer generates a more evenly distributed temperature across its cross-section. It maintains a lower wall temperature, even when subjected to the same incoming heat flux. In contrast to the empty SAH, the porous solar heater demonstrates a more uniform temperature distribution, with a lower temperature observed on the lower wall ($H = 0$). Notably, as the metal foam height increases, the porous layer's temperature distribution becomes more uniform. The high thermal conductivity of the porous media and the mechanical mixing within the porous layer contributes to an enhanced heat transfer rate from the absorber wall, resulting in lower temperatures of the absorber plate.

A decline in temperature is evident in Figure 10b as the Reynolds number increases. According to the principle of energy conservation within SAH, $Q = \dot{m}\, c_P(T_o - T_i)$, increasing the velocity and Re results in a higher mass flow rate, which results in a decrease in the temperature difference between the input and output while keeping the amount of heat transmitted to the SAH constant, Q. As the inlet temperature (T_i) is constant, the outlet temperature (T_o) diminishes as Re increases.

The temperature profiles across the height of the SAH duct for different pore densities are presented in Figure 10c for $H_f = 0.6$. The temperature variation across the channel height is slightly higher for 40 PPI compared to other PPIs of metallic foam in the porous zone, whereas it decreases in the open zone. As the pore size increases, the velocity decreases within the foam-filled region and rises in the fluid region. An increase in flow velocity within the fluid region reduces the time of contact between the air and the heat source. Consequently, the air's capacity to assimilate the entire quantity of heat diminishes. This effect occurs due to the increased air velocity inside the system, reducing the time for thermal contact. This, in turn, leads to a reduction in the variance in exit temperature at the larger PPI of the metallic foam. In other words, as the air moves faster, it absorbs less heat, resulting in fewer temperature variations between various exit points.

4.3 TKE production

The Turbulent Kinetic Energy (TKE) contours inside the heater for different foam heights and Re = 16000 are shown in Figure 11. As the porous-fluid interface experiences a greater velocity gradient, an elevated degree of turbulent kinetic energy (TKE) generation was noticed at this location. Moreover, Figure 11 demonstrates that the k_ε model accurately represents the higher TKE level near the porous/fluid interface compared to the TKE near the solid top wall. The profiles produced by Breugem and Boersma [56] exhibit excellent agreement. The magnitude of turbulent kinetic energy (TKE) is negligible within the porous medium; however, it gradually rises to its maximum value at the interface between the porous material and the fluid. The TKE drops as it approaches a lower maximum at the top wall, followed by a continuing decline along the wall.

According to Chandesris et al. [57], a disparity in velocity between the fluid inside and outside of a porous layer induces Kelvin-Helmholtz instabilities at the interface, generating significant turbulence patterns across the permeable wall. The peaks observed in the turbulent kinetic energy (TKE) profiles at the interface between the porous medium and the fluids in Figure 12a represent this impact. These peaks are substantially greater than those near the channel's upper solid wall. Furthermore, creating these big structures in the channel's clear section promotes turbulence mixing, which improves heat transmission between the main flow and the heated plate. Figure 12b illustrates the turbulent kinetic energy (TKE) across the channel height at x =L_1+L_2⁄2 with a pore density of 10 PPI while considering various Re numbers. Regardless of the Reynolds number, there is only one singular point of maximal turbulent kinetic energy (TKE) at the interface between the porous material and the fluid. This indicates a regular trend in which TKE attains its maximum value at a certain place within the interface. As Re grows, the peak of the turbulent kinetic energy distribution similarly increases. The relationship between Re and turbulent kinetic energy suggests that greater fluid flow rates, which correspond to higher Reynolds numbers, lead to an augmentation of turbulent kinetic energy at the interface between the porous material and the fluid. Figure 12c displays the effect of pore density on TKE. It can be seen that the TKE profiles have an upward relationship with pore density, as indicated by the increasing peak values. Increased pore density reduces the permeability of the foam structure, resulting in greater resistance to fluid movement. Consequently, the contrast in fluid velocities between the porous layer and its surroundings increases, as depicted in Figure 7. This leads to intensified turbulence effects at the interface when the pore density is higher.

4.4 Heat Transfer Characteristics

Within the metal foam region, there are two potential routes for the transfer of heat delivered to the channel wall: firstly, it can be directly transmitted to the fluid, or secondly, it can be conducted via the metal foam fibers and subsequently transferred to the fluid through convective heat transfer. Therefore, the thermal resistances can be categorized into three components:

1. The convective thermal resistance existing between the heated plate and the fluid
2. The conductive thermal resistance of the solid material
3. The thermal local convective resistance occurring between the solid and the fluid

Both the metal foam and fluid components contribute to the overall thermal resistance. Thermal energy is transferred from the metal-foam region to the fluid in the non-metal-foam region within the open zone [58,59].

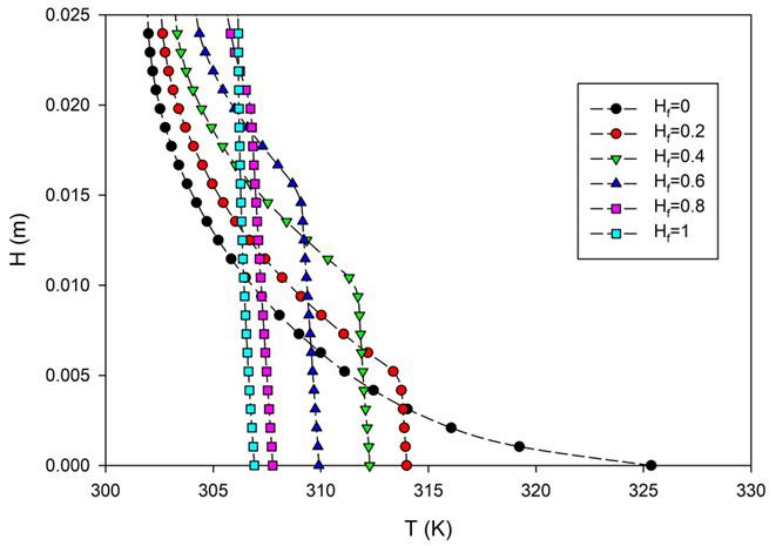

(a)

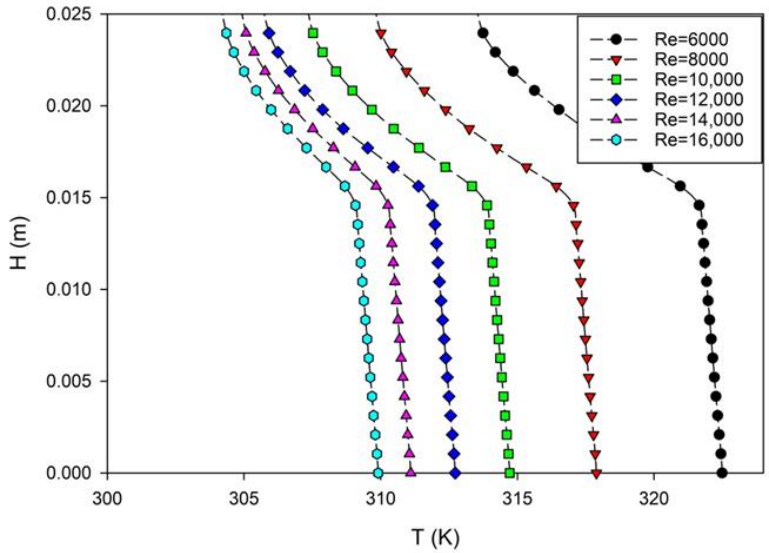

(b)

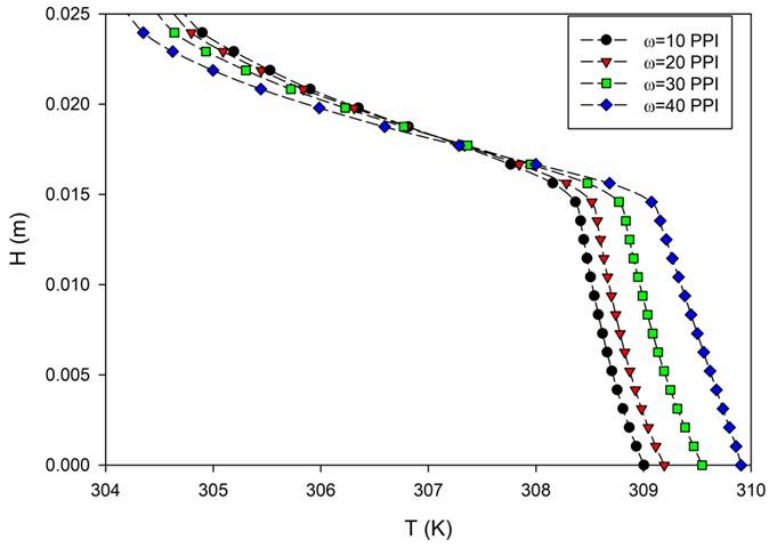

(c)

Figure 10: Impacts of key factors on temperature distribution along the SAH duct high: (a) foam height, (b) Re, and (c) pore density

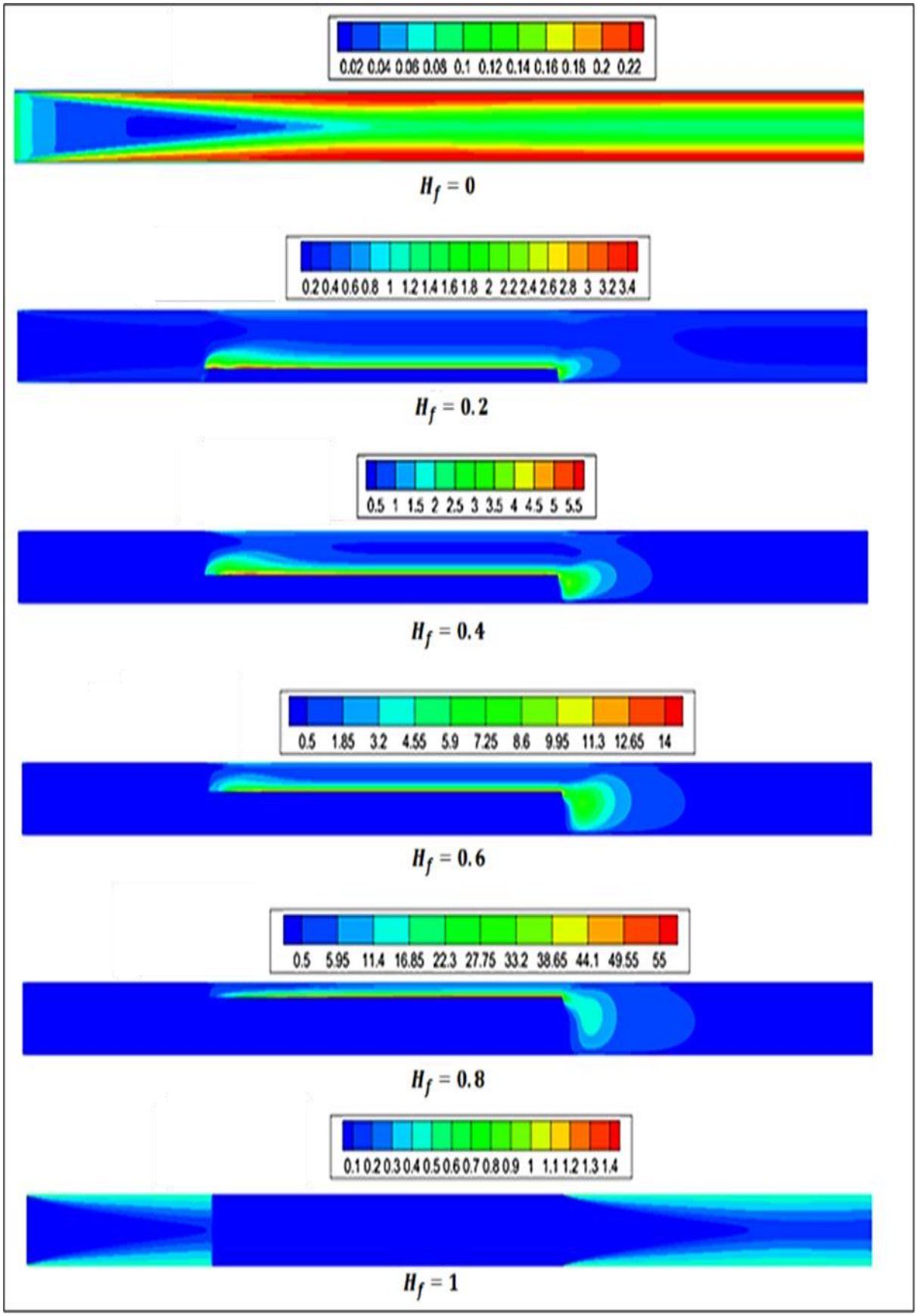

Figure 11: TKE contours inside the heater at Re = 16000 for different dimensionless foam heights

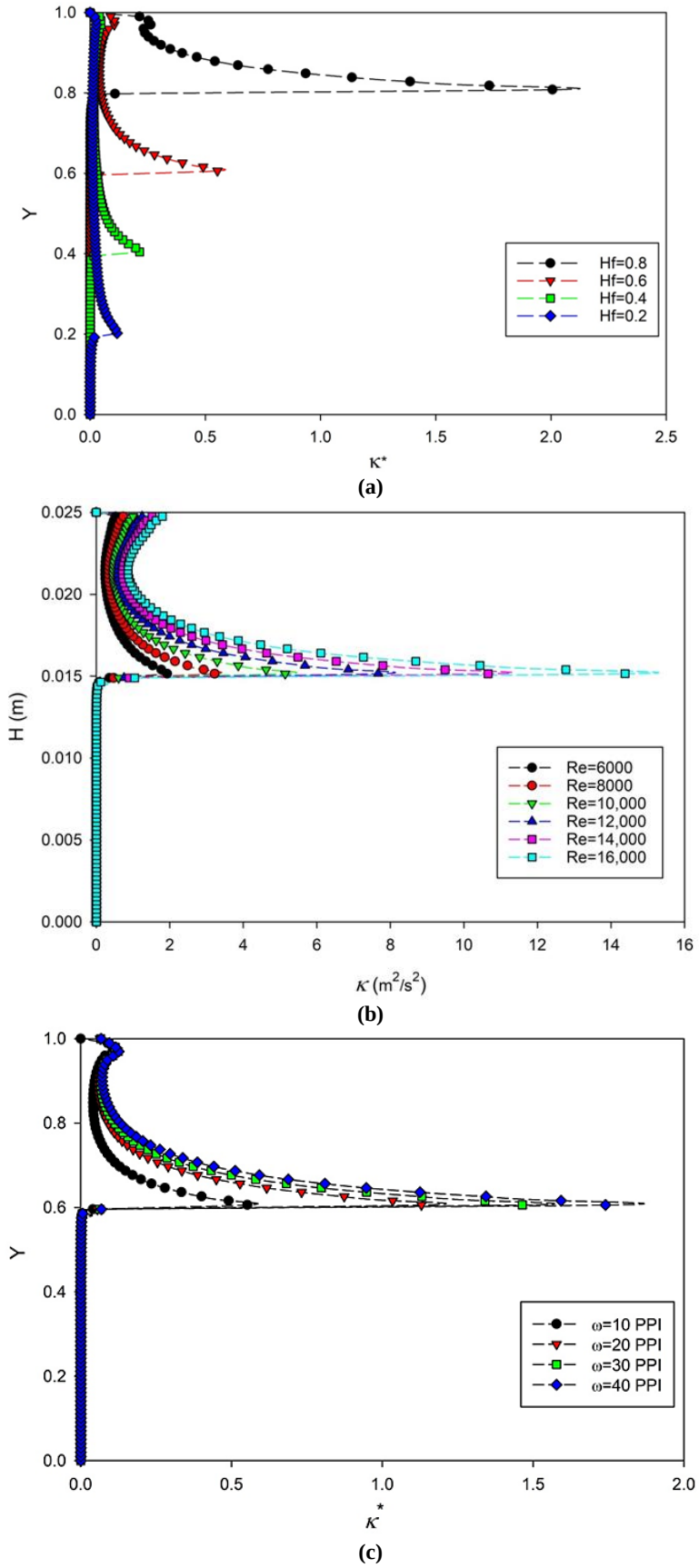

Figure 12: Impacts of key factors on TKE production: (a) foam height, (b) Re, and (c) pore density

4.4.1 The effect of foam height

In Figure 13, the impacts of vital parameters on average Nu are illustrated. The Nu number exhibits an upward trend with the thicker foam across various Re values, as illustrated in Figure 13a. The high thermal conduction effect of the metal

foam, as well as the higher surface area and better fluid mixing, allows for efficient transfer of heat from the wall to the moving fluid. Furthermore, the Nu number rises in conjunction with the Re for various foam heights, as an increase in Re number can facilitate convection heat transmission and decrease the thermal resistance of the fluid component. The thermal resistance of the fluid component diminishes and loses prominence as the Re number rises. The obtained Nu values for the SAH with the metal foam are 3.6 to 18.04 times higher than those of the SAH without foam, considering the Re numbers and foam height under consideration. Furthermore, at Re of 16000, the Nu increases by 309.9% as H_f increased from 0.2 to 1. While the Nu increases by only 122% as Re increased from 6000 to 16,000 for $H_f = 1$. This implies that altering the height of the metal foam has a more noticeable impact on the heat transfer improvement (as shown by Nu) compared to increments in the flow rate of the fluid (Re).

4.4.2 The effect of pore density

Figure 13b depicts the influence of pore density on average Nu for various Re at $H_f = 0.6$. It is also discovered that when pore density rises, the Nu eventually declines to a nearly constant value. This pattern is remarkably similar to previous studies, such as Xia et al. [1,38] and Nimvari et al. [60]. Although growing pore density at a fixed porosity can enhance heat transmission surface area, the mass flow within the foam zone drastically reduces. Therefore, the local area's convective thermal resistance increases as the foam zone's mass flow rate decreases. Still, the thermal resistance owing to heat conduction remains unchanged (fixed porosity). At a large pore density, the declining trend of the mass flow in the foam zone becomes less pronounced, resulting in a constant Nu number. Therefore, it is recommended to use a moderate pore density in the thermal design of associated applications to optimize heat transfer performance and minimize pressure loss. At $H_f = 0.6$, and $Re = 16{,}000$, the 10 PPI copper metal foam exhibits 960.4% in Nu compared to the empty SAH and 19.37% compared to 40 PPI.

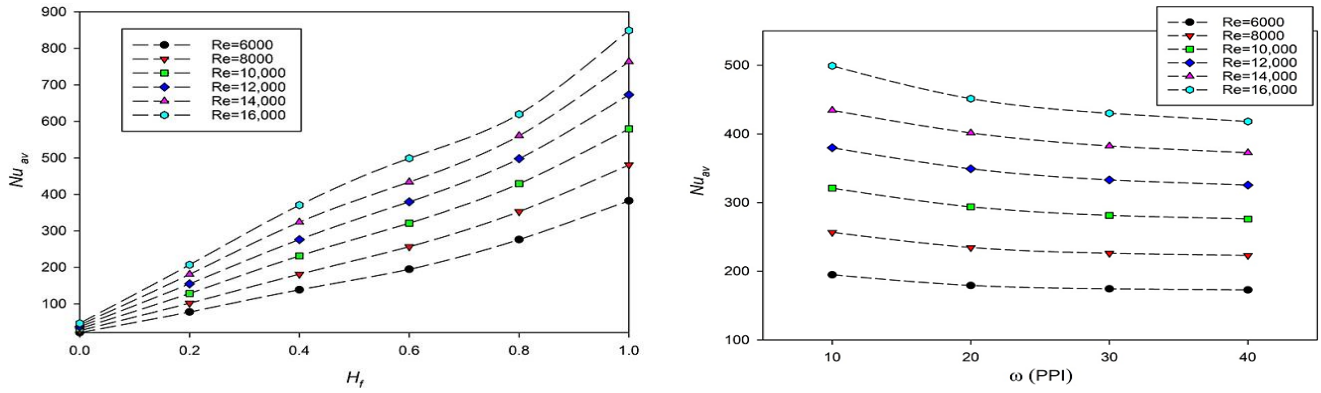

(a) (b)

Figure 13: Impacts of key factors on heat transfer features: (a) foam height and (b) pore density

4.5 Pressure drop

4.5.1 The effect of foam height

The increasing trend in pressure drop is a critical consideration when utilizing a porous material to improve heat transfer. Figure 14a depicts the effect of dimensionless foam height (H_f) on friction factor for various Reynolds numbers at $\omega = 10\ PPI$.

The pressure drop increases as the height of the metal foam area grows. The larger the foam height, the higher the pressure drop; the higher the incoming air velocity, the higher the pressure drop. Increased porous layer height reduces the transparent fluid area and hardens fluid flow, increasing pressure drop. Furthermore, the impact of Re is sensitive to foam height; that is, the higher H_f, the greater the influence of Re. The pressure loss for a channel configuration with full metal foam content is significantly greater than that of a channel with a partial porous material fill. Including metal foam increases the pressure drop by around 5-490 times compared to an empty SAH duct for the range of foam heights examined.

4.5.2 The effect of pore density

As indicated in Figure 14b, the pressure drop increases as pore density rises. In this case, the higher PPI causes the fiber diameter of the metallic foams to decrease, increasing the foam's inertial resistance and, as a result, the pressure drop.

Additionally, the increment rate diminishes as the pore density grows. When the pore density increases, the resistance within the foam zone forces a greater volume of fluid to pass within the open zone. As a result, the pressure drop is less affected by the growing pore density. At Re=16000, the pressure drop increased by 41.14% as pore density rose from 10PPI to 20 PPI. Farther the pore density to 40 PPI increases the pressure drop by only 31.72%. Moreover, the variation in ΔP

between two PPIs grows as Re increases. At Re=6000, the pressure drop increased by 61.13% as the pore density increased from 10 PPI to 40 PPI. Increasing Re to 16,000, the pressure drop increases by 85.92% for the same pore density range.

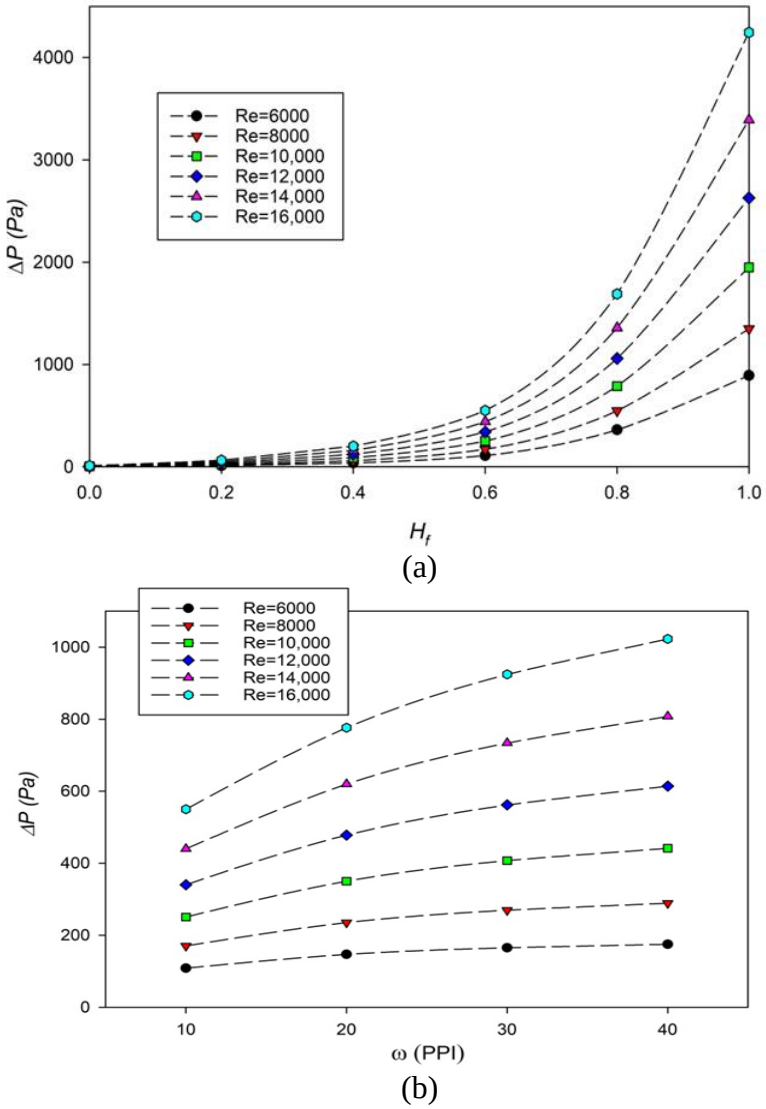

Figure 14: Impacts of key factors on pressure drop: (a) foam height and (b) pore density

4.6 Friction Factor

As previously established, foam height, Re, and pore density are all significant factors in identifying flow characteristics. The impacts of these factors on the friction factor are investigated in this section and illustrated in Figure 15.

4.6.1 The effect of foam height

The influence of dimensionless foam height (H_f) on friction factor for various Re numbers is shown in Figure 15a. As expected, when H_f climbs from 0 to 1, the friction factor goes up from the value of an empty channel to that of a channel filled with metallic foam. As H_f goes up, the area of the low-permeability zone also expands and contributes to the rising trend. It is important to highlight that the friction factor (f) consistently exhibits higher values at lower Re numbers. According to the definition of the friction factor in Equation (21), at small Re numbers, the flow rate in the SAH channel is low, indicating lower total flow kinetic energy. Consequently, the friction factor tends to be higher under these conditions.

4.6.2 The effect of pore density

Figure 15b illustrates the impact of pore density on the f for various Re numbers. The friction factor exhibits a significant rise with increasing pore density due to the reduction in permeability of porous foam. However, it eventually levels out as ω continues to grow. This phenomenon may be explained by the decrease in mass flow fraction in the foam zone when ω reaches a high enough level. This indicates that the porous structure has little impact on flow resistance after the pore density is above a certain threshold.

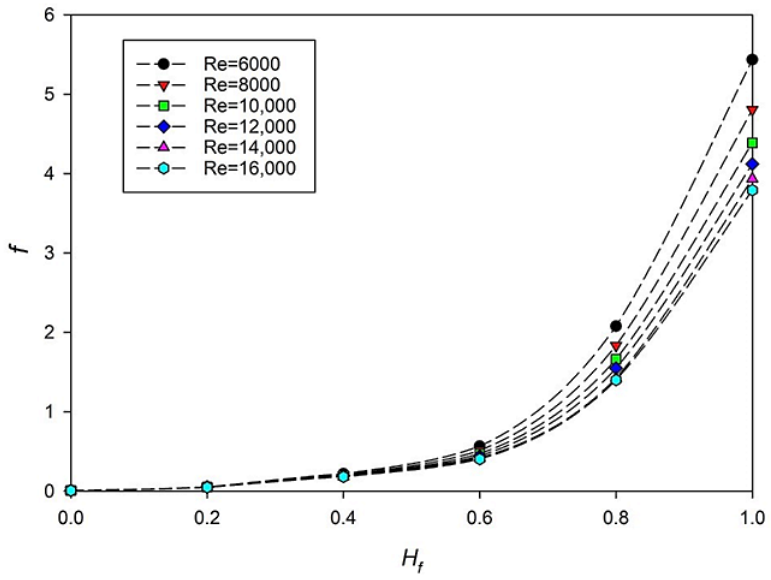

(a)

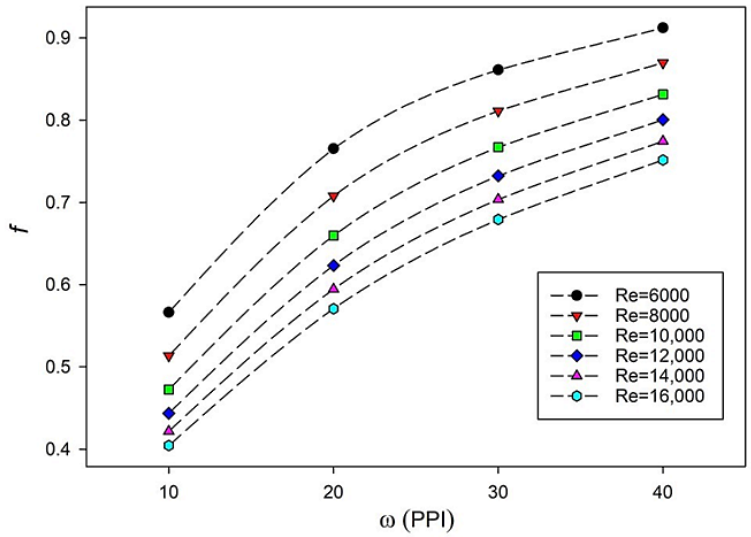

(b)

Figure 15: Impacts of key factors on friction factor: (a) foam height and (b) pore density

4.7 Thermal performance factor

The TPF, as specified in Equation (9), evaluates the overall performance of the SAH system by considering the pressure drop increase and heat transfer enhancement. It is accepted that the TPF value will be greater than 1, indicating that the impact of improved heat transfer surpasses that of increasing pressure drop.

The effects of dimensionless foam height, pore density, and Re number on the TPF values of the enhanced SAH system are illustrated in Figure 16 (a,b). The Figure illustrates that the TPF values for the range of dimensionless foam heights, pore densities, and Re numbers examined are consistently greater than 1. This indicates that the enhanced SAH possesses a substantial application value. Moreover, as shown in Figure 16 (a), initially, as the dimensionless foam height increases, the TPF values rise. This suggests an improvement in performance with a certain range of foam height. The TPF values reach their peak values at a certain dimensionless foam height. This indicates an optimal height for the foam layer, maximizing the system's performance. As the dimensionless foam height increases beyond the optimum value, the TPF values begin to drop. The decline in performance might be ascribed to diminished returns or negative impacts on the heat transfer mechanism caused by excessively thicker foam layers. It is found that $H_f = 0.6$ is an optimum porous layer height for all of Re numbers that are in accordance with Nimvari et al. [60] results. When theH_f value exceeds 0.6, the rise in the resistance coefficient (f) is greater than the increase in the Nu number. Consequently, the enhanced SAH system under this condition has less practical utility. As the metal foams cover the entire absorber plate area (see Figure 1b) and the thinner foam height will not considerably increase the pressure drop, it is noted that $H_f = 0.6$ and $\omega = 10\ PPI$, the TPF ranges from 2.33 to 2.82, showing a superior thermo-hydraulic performance.

Further, it shows that TPF increases with Re for a constant foam height but decreases with pore density for the same foam height and Re. This pattern is similar to that observed by Jouybari and Lundström [23]. The impact of increasing the Re on the

Nu is highly evident. However, it has a little impact on the Darcy and inertial resistances in the porous zone, likewise the shear stress in the non-porous zone. Thus, the overall effect is a rise in the TPF values.

In addition, as mentioned previously, the Nu decreases while friction increases with pore density. Therefore, it is intuitive that the TPF decreases with increasing pore density, as shown in Figure 16 (b). The TPF drops sharply at low pore densities; however, it decreases less slowly as the pore density continues to grow. At Re=16000, the TPF drops from 2.82 to 2.27 and from 2.27 to 1.92 as pore density increases from 10 to 20 PPI and from 20 to 40 PPI, respectively.

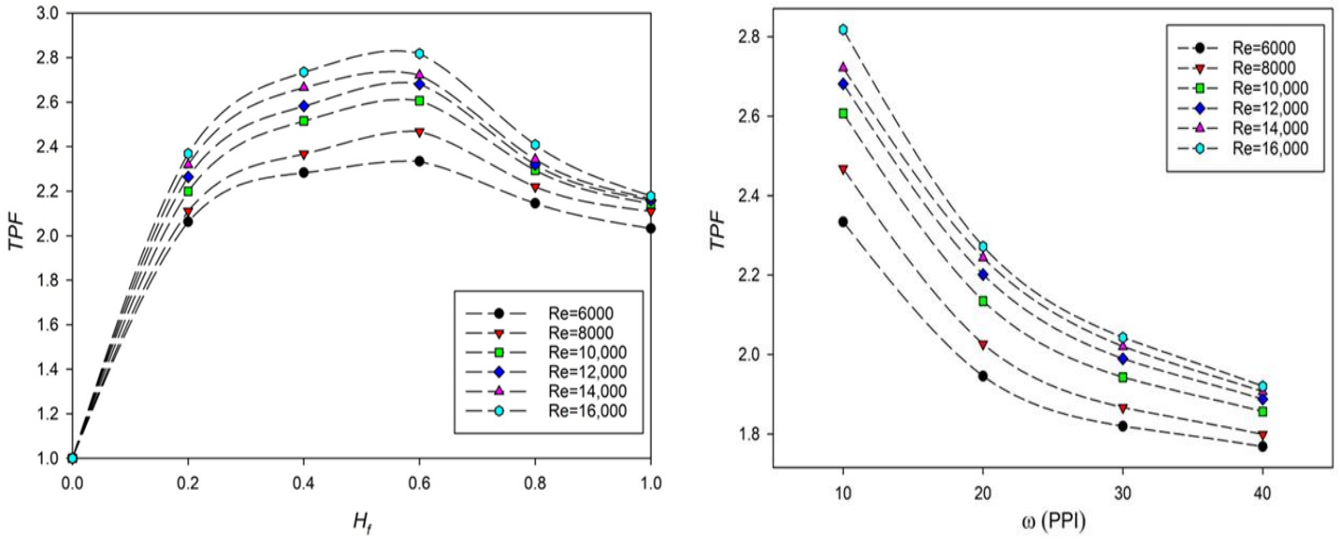

(a) **(b)**

Figure 16: Impacts of key factors on TPF: (a) foam height (b) pore density

4.8 Development of correlations for average Nu and f

At a constant foam height, the average Nu and f are strong functions of Reynolds number (Re) and pore density (ω). The functional relationships of Nu and f in terms of Re and ω are therefore given as,

$$Nu = f_n(Re, \omega) \tag{25}$$

$$f = f_n(Re, \omega) \tag{26}$$

To acquire the necessary correlations, a non-linear regression analysis was conducted on computational data, following the procedure of [61]. The following correlations for Nu and f were determined from the regression analysis:

$$Nu = 0.07473 \times \omega^{-0.1097} \times Re^{0.9343} \tag{27}$$

$$f = 2.2901 \times \omega^{0.4126} \times Re^{-0.2727} \tag{28}$$

The comparisons of Nu and f obtained from the present numerical investigations and that predicted by the empirical correlations above are shown in Figure 17 (a and b). All the predicted data points were found within ± 2% for Nu and ± 5% for the friction factor range of the numerical values. In other words, within the specified parameter ranges, the suggested correlations or models for predicting Nu and friction loss are dependable and accurate.

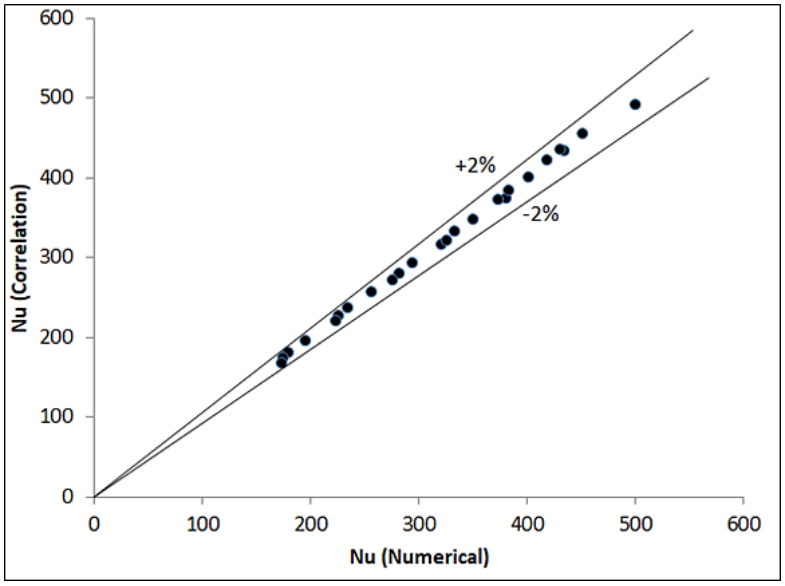

(a)

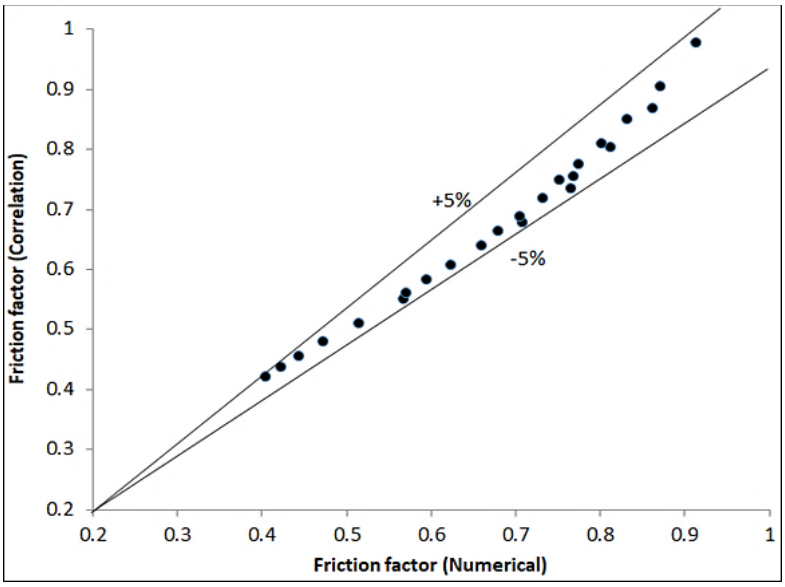

(b)

Figure 17: Comparisons of the numerical and the predicted data for (a) Nu and (b) f

5. Conclusion

In this study, computational simulations were conducted using the commercially available ANSYS Fluent 2023 R1 software to analyze the flow and heat transfer characteristics in a Solar Air Heater (SAH) channel partially filled with copper metal foam. Metal foam with high thermal conductivity was positioned on the absorber plate to improve heat transfer. The investigation includes a detailed analysis of the effects of metal foam height, permeability, and Reynolds number on velocity and temperature profiles, flow resistance coefficient (f), Nusselt number (Nu), and Thermo-hydraulic Performance Factor (TPF). The preexisting experimental data were used to support the proposed investigation. The present numerical analysis concludes with the following remarks:

1) Integrating metal foam characterized by high thermal conductivity and porosity into the SAH duct results in more even temperature distributions within the foam area. This leads to a reduction in the temperature of the absorber plate and, consequently, a significant enhancement in heat transmission.
2) With an increase in Reynolds number (Re), there is a proportional rise in velocity distribution throughout the channel height, observed in both porous and non-porous regions. Nevertheless, as Re increases, the channel discharge and absorber plate temperature decreases. This is attributed to the greater fluid flow through the foam zone.
3) The Nusselt number (Nu) exhibits an increasing trend with the height of the metal foam substrate, as indicated across the range of Reynolds numbers and pore densities examined. These enhancements are noted to be 4.4, 7.87, 10.6, 13.17 and 18.04 times for $H_f = 0.2, 0.4, 0.6, 0.8, and\ 1$, respectively at $\omega = 10PPI$. Nevertheless, the

deterioration of Nu is observed with an increase in pore density, where the Nu fell by 19.38% as the pore density increased from 10 PPI to 40 PPI.

4) An increase in foam pore density and foam height leads to an increase in the friction factor. The friction factor increased by 46% as the pore density increased from 10 PPI to 40 PPI. On the other hand, the friction factor reduces as the Reynolds number increases. At $H_f = 0.6$ and $\omega = 10PPI$, the friction factor reduced by about 28.6% as Re number increased from 6000 to 16000.
5) When assessing the overall performance, the TPF takes a pressure-drop penalty and heat transmission improvement into account. The highest thermal performance is achieved at $H_f = 0.6$. The Nu increases approximately 9-10.6 times, while the f increases by 53.5-56.6 times, compared to the empty SAH duct. The TPF ranges from 2.33 to 2.82 for $H_f = 0.6$ and $\omega = 10\ PPI$.

Nomenclature

a_{sf}	Specific surface area, m^{-1}
C	Forchheimer coefficient
$C_{\varepsilon 1}, C_{\varepsilon 2}, C_\mu, \sigma_k, \sigma_\epsilon$	Constants in the k _ ε turbulent model
D_h	Hydraulic diameter, m
d_p	Pore diameter (m)
d_f	fiber diameter (m)
f	Friction factor
h	Heat transfer coefficient, $Wm^{-2}\ K^{-1}$
H	Duct height (m)
h_f	Metal foam height (m)
$H_f = h_f/H$	Dimensionless Metal foam height
K	Permeability (m^2)
k	Turbulent kinetic energy (m^2/s^2)
$k^* = {k}/{u_{av}{}^2}$	Non-dimensional turbulent kinetic energy
L_1	Entrance section length (m)
L_2	Test section length (m)
L_3	Exit section length (m)
$Nu = \frac{\bar{h}\, D_h}{\lambda_f}$	Nusselt number
P	Pressure (Pa)
$Re = \frac{\rho\, u_{av} D_h}{\mu_f}$	Reynolds number
T	Temperature (K)
u, v	Velocity component, m s^{-1}
$u^* = {u}/{u_{av}}$	Non-dimensional axial velocity
x, y	Cartesian coordinates (m)
X, Y	Non-dimensional Cartesian coordinates, $X = x/L_2$, $Y = y/H$

Greek symbols

ρ	density, kg/m^3
μ	dynamic viscosity, kg. $m^{-1}.s^{-1}$
Ø	porosity
ω	Pore density, PPI
λ	Thermal conductivity, $Wm^{-1}\ K^{-1}$
ε	Dissipation rate of k, (m^2s^{-3})

Abbreviations

DEF	Darcy-Extended Forchheimer model
FPSC	Flat-plate solar collector
LTE	Local thermal equilibrium
LTNE	Local thermal non-equilibrium
PEC	Performance evaluation criteria
PPI	Pore per inch
SAH	Solar air heater
TPF	Thermal performance factor

Subscripts

av	average
s	smooth duct, solid
f	fluid
e	effective
i	inlet
o	outlet

Author contributions

Conceptualization, K. Al-Chlaihawi, M. Hasan and A. Ekaid; methodology, K. Al-Chlaihawi; software, K. Al-Chlaihawi and A. Ekaid; validation, K. Al-Chlaihawi; formal analysis, K. Al-Chlaihawi, M. Hasan and A. Ekaid; investigation, K. Al-Chlaihawi and M. Hasan; resources, K. Al-Chlaihawi; data curation, K. Al-Chlaihawi; writing—original draft preparation, K. Al-Chlaihawi; writing—review and editing, K. Al-Chlaihawi and M. Hasan; visualization, K. Al-Chlaihawi, M. Hasan and A. Ekaid; supervision, M. Hasan and A. Ekaid; project administration, M. Hasan and A. Ekaid. All authors have read and agreed to the published version of the manuscript.

Funding

This research received no specific grant from any funding agency in the public, commercial, or not-for-profit sectors.

Data availability statement

The data that support the findings of this study are available on request from the corresponding author.

Conflicts of interest

The authors declare that there is no conflict of interest.

References

[1] Y. F. Xia, et al., Enhanced thermal performance of a flat-plate solar collector inserted with porous media: A numerical simulation study, Therm. Sci. Eng. Prog., 44 (2023) 102063. https://doi.org/10.1016/j.tsep.2023.102063

[2] Z. Liu, et al., Game theory-based renewable multi-energy system design and subsidy strategy optimization, Adv. Appl. Energy, 2 (2021) 100024. https://doi.org/10.1016/j.adapen.2021.100024

[3] Yan, J., Energy systems in transition: challenges and opportunities, Adv. Appl. Energy, 1 (2020) 100005. http://dx.doi.org/10.1016/j.adapen.2020.100005

[4] S. A. Sakhaei, and M.S. Valipour, Performance enhancement analysis of The flat plate collectors: A comprehensive review, Renewable Sustainable Energy Rev., 102 (2019) 186-204. https://doi.org/10.1016/j.rser.2018.11.014

[5] Choudhury, P.K. and D.C. Baruah, Solar air heater for residential space heating, Energy Ecol. Environ., 2 (2017) 387-403. https://doi.org/10.1007/s40974-017-0077-4

[6] A. Saxena, et al., Experimental studies of latent heat storage based solar air heater for space heating: A comparative analysis, J. Build. Eng., 69 (2023) 106282. https://doi.org/10.1016/j.jobe.2023.106282

[7] A. Al-damook, and W.H. Khalil, Experimental evaluation of an unglazed solar air collector for building space heating in Iraq, Renewable Energy, 112 (2017) 498-509. https://doi.org/10.1016/j.renene.2017.05.051

[8] D. Kumara, et al., Performance improvement of a solar desalination system assisted with solar air heater: An experimental approach, J. Indian Chem. Soc., 79 (2020) 1967-1972.

[9] O. García-Valladares, et al., Solar thermal drying plant for agricultural products. Part 1: Direct air heating system. Renewable Energy, 148 (2020) 1302-1320. https://doi.org/10.1016/j.renene.2019.10.069

[10] A. Lingayat, R. Zachariah, and A. Modi, Current status and prospect of integrating solar air heating systems for drying in various sectors and industries, Sustainable Energy Technol. Assess., 52 (2022) 102274. https://doi.org/10.1016/j.seta.2022.102274

[11] S. Gorjian, et al., A review on recent advancements in performance enhancement techniques for low-temperature solar collectors, Energy Convers. Manage., 222 (2020) 113246. https://doi.org/10.1016/j.enconman.2020.113246

[12] K. K. Al-Chlaihawi, M.R. Hasan, and A.L. Ekaid, Compound passive heat transfer augmentation techniques: A comprehensive review, Heat Transfer.53 (2023) 363-421. https://doi.org/10.1002/htj.22955

[13] C. Prakash, and R.P. Saini, Use of artificial roughness for performance enhancement of solar air heaters—a review. Int. J. Green Energy, 16 (2019) 551-572. https://doi.org/10.1080/15435075.2019.1598418

[14] K. K. Al-Chlaih awi, K.K.I., M.R. Hasan, and A.L. Ekaid, Thermohydraulic performance assessment of a solar air heater with equilateral-triangular, trapezoidal, and square sectional ribs on the absorber plate: A comparative study, Heat Transfer, 53 (2023) 441-471. https://doi.org/10.1002/htj.22958

[15] K. K. Al-Chlaihawi, B.H. Alyas, and A.A. Badr, CFD Based Numerical Performance Assessment of a Solar Air Heater Duct Roughened by Transverse-Trapezoidal Sectioned Ribs, Int. J. Heat Technol., 41 (2023) 1273-1281, https://doi.org/10.18280/ijht.410517

[16] N. H. Abu-Hamdeh, R.A. Alsulami, and R.I. Hatamleh, A case study in the field of building sustainability energy: Performance enhancement of solar air heater equipped with PCM: A trade-off between energy consumption and absorbed energy, J. Build. Eng., 48 (2022) 103903. https://doi.org/10.1016/j.jobe.2021.103903

[17] J. Assadeg, et al., Energetic and exergetic analysis of a new double pass solar air collector with fins and phase change material, Sol. Energy, 226 (2021) 260-271. https://doi.org/10.1016/j.solener.2021.08.056

[18] R. Kumar, S. Kumar Verma, and V. Kumar Sharma, Performance enhancement analysis of triangular solar air heater coated with nanomaterial embedded in black paint, Mater. Today: Proc., 26 (2020) 2528-2532. https://doi.org/10.1016/j.matpr.2020.02.538

[19] R. Kumar, and P. Chand, Performance enhancement of solar air heater using herringbone corrugated fins, Energy, 127 (2017) 271-279. https://doi.org/10.1016/j.energy.2017.03.128

[20] V. C. Ifrim, and O.V. Grosu. Review of thermal performance enhancement of Solar Air Heater using baffles on absorber plate, International Conference on Development and Application Systems (DAS). 2022. IEEE. https://doi.org/10.1109/DAS54948.2022.9786129

[21] S. Chand, P. Chand, and H. K. Ghritlahre, Thermal performance enhancement of solar air heater using louvered fins collector, Sol. Energy, 239 (2022) 10-24. https://doi.org/10.1016/j.solener.2022.04.046

[22] O. Zhu, and Y. Xuan, Pore scale numerical simulation of heat transfer and flow in porous volumetric solar receivers, Appl. Therm. Eng., 120 (2017) 150-159. https://doi.org/10.1016/j.applthermaleng.2017.03.141

[23] N. F. Jouybari, and T.S. Lundström, Performance improvement of a solar air heater by covering the absorber plate with a thin porous material, Energy, 190 (2020) 116437. https://doi.org/10.1016/j.energy.2019.116437

[24] Z. Chen, M. Gu, and D. Peng, Heat transfer performance analysis of a solar flat-plate collector with an integrated metal foam porous structure filled with paraffin, Appl. Therm. Eng., 30 (2010) 1967-1973. https://doi.org/10.1016/j.applthermaleng.2010.04.031

[25] S. Rashidi, M. Bovand, and J.A. Esfahani, Heat transfer enhancement and pressure drop penalty in porous solar heat exchangers: A sensitivity analysis, Energy Convers. Manage., 103 (2015) 726-738. https://doi.org/10.1016/j.enconman.2015.07.019

[26] M. Bovand, S. Rashidi, and J.A. Esfahani, Heat transfer enhancement and pressure drop penalty in porous solar heaters: Numerical simulations, Sol. Energy, 123 (2016) 145-159. https://doi.org/10.1016/j.solener.2015.10.054

[27] M. T. Jamal-Abad, S. Saedodin, and M. Aminy, Heat transfer in concentrated solar air-heaters filled with a porous medium with radiation effects: A perturbation solution, Renewable Energy, 91 (2016) 147-154. https://doi.org/10.1016/j.renene.2016.01.050

[28] H. J. Jouybari, et al., Experimental investigation of thermal performance and entropy generation of a flat-plate solar collector filled with porous medial, Appl. Therm. Eng., 127 (2017) 1506-1517. https://doi.org/10.1016/j.applthermaleng.2017.08.170

[29] S. Saedodin, et al., Performance evaluation of a flat-plate solar collector filled with porous metal foam: Experimental and numerical analysis, Energy Convers. Manage., 153 (2017) 278-287. https://doi.org/10.1016/j.enconman.2017.09.072

[30] H. J. Jouybari, et al., Effects of porous material and nanoparticles on the thermal performance of a flat plate solar collector: An experimental study, Renewable Energy, 114 (2017) 1407-1418. https://doi.org/10.1016/j.renene.2017.07.008

[31] H. J. Jouybari, et al., Analytical investigation of forced convection heat transfer in a flat-plate solar collector filled with a porous medium by considering radiation effect, J. Porous Media, 21 (2018). http://dx.doi.org/10.1615/JPorMedia.2018028768

[32] Valizade, M., M. Heyhat, and M. Maerefat, Experimental study of the thermal behavior of direct absorption parabolic trough collector by applying copper metal foam as volumetric solar absorption, Renewable Energy, 145 (2020) 261-269. https://doi.org/10.1016/j.renene.2019.05.112

[33] K. Anirudh, and S. Dhinakaran, Performance improvement of a flat-plate solar collector by inserting intermittent porous blocks, Renewable Energy, 145 (2020) 428-441. https://doi.org/10.1016/j.renene.2019.06.015

[34] K. Anirudh, and S. Dhinakaran, Numerical analysis of the performance improvement of a flat-plate solar collector using conjugated porous blocks, Renewable Energy, 172 (2021) 382-391. https://doi.org/10.1016/j.renene.2021.02.145

[35] R. Diganjit, N. Gnanasekaran, and M. Mobedi, Numerical Study for Enhancement of Heat Transfer Using Discrete Metal Foam with Varying Thickness and Porosity in Solar Air Heater by LTNE Method, Energies, 15 (2022) 8952. https://doi.org/10.3390/en15238952

[36] K. G. Fadhala, E.M. Fayyadh, and A.F. Mohammed, Experimental investigation on the thermal-hydraulic performance of channel with gradient metal foam baffles, FME Transactions, 51 (2023) 14-22. https://doi.org/10.5937/fme2301014F

[37] Y. Fu, et al., A novel structure design and numerical analysis of porous media-assisted enhanced thermal performance of flat-plate solar collector, Therm. Sci. Eng. Prog., 40 (2023) 101777. https://doi.org/10.1016/j.tsep.2023.101777

[38] Y. Xia, et al., Numerical Study on the Enhanced Thermal Performance of the Porous Media-Assisted Flat-Plate Solar Collector, Int. J. Energy Res., 2023 (2023) 2244771. https://doi.org/10.1155/2023/2244771

[39] A. A. Handbook, and G. Atlanta, UAS: American Society of Heating, Refrigerating and Air Conditioning Engineers, 2003.

[40] V. V. Calmidi, and R.L. Mahajan, Forced convection in high porosity metal foams. J. Heat Transfer, 122 (2000) 557-565. https://doi.org/10.1115/1.1287793

[41] B. Alazmi, and K. Vafai, Constant wall heat flux boundary conditions in porous media under local thermal non-equilibrium conditions, Int. J. Heat Mass Transfer, 45 (2002) 3071-3087. https://doi.org/10.1016/S0017-9310(02)00044-3

[42] J. Liu, G. Xie, and T.W. Simon, Turbulent flow and heat transfer enhancement in rectangular channels with novel cylindrical grooves, Int. J. Heat Mass Transfer, 81 (2015) 563-577. https://doi.org/10.1016/j.ijheatmasstransfer.2014.10.021

[43] Y. M. Patel, S.V. Jain, and V.J. Lakhera, Thermo-hydraulic performance analysis of a solar air heater roughened with reverse NACA profile ribs, Appl. Therm. Eng., 170 (2020) 114940. https://doi.org/10.1016/j.applthermaleng.2020.114940

[44] R. Webb, and E. Eckert, Application of rough surfaces to heat exchanger design, Int. J. Heat Mass Transfer, 15 (1972) 1647-1658. https://doi.org/10.1016/0017-9310(72)90095-6

[45] P. H. Jadhav, and N. Gnanasekaran, Optimum design of heat exchanging device for efficient heat absorption using high porosity metal foams, Int. Commun. Heat Mass Transfer, 126 (2021) 105475. https://doi.org/10.1016/j.icheatmasstransfer.2021.105475

[46] R. M. K. Ali, and S.L. Ghashim, Numerical analysis of the heat transfer enhancement by using metal foam, Case Stud. Therm. Eng., 49 (2023) 103336. https://doi.org/10.1016/j.csite.2023.103336

[47] B. Kotresha, and N. Gnanasekaran, Numerical simulations of fluid flow and heat transfer through aluminum and copper metal foam heat exchanger–a comparative study, Heat Transfer Eng., 41 (2019) 637-649. https://doi.org/10.1080/01457632.2018.1546969

[48] W. Lin, et al., Comparison and analysis of heat transfer in aluminum foam using local thermal equilibrium or non-equilibrium model, Heat Transfer Eng., 37 (2016) 314-322. https://doi.org/10.1080/01457632.2015.1052682

[49] V. V. Calmidi, Transport phenomena in high porosity fibrous metal foams. 1998: University of Colorado at Boulder.

[50] W. Lu, C. Zhao, and S. Tassou, Thermal analysis on metal-foam filled heat exchangers. Part I: Metal-foam filled pipes, Int. J. Heat Mass Transfer, 49 (2006) 2751-2761. https://doi.org/10.1016/j.ijheatmasstransfer.2005.12.012

[51] K. Boomsma, and D. Poulikakos, On the effective thermal conductivity of a three-dimensionally structured fluid-saturated metal foam, Int. J. Heat Mass Transfer, 44 (2001) 827-836. https://doi.org/10.1016/S0017-9310(00)00123-X

[52] N. Dukhan, Ö. Bağcı, and M. Özdemir, Thermal development in open-cell metal foam: An experiment with constant wall heat flux, Int. J. Heat Mass Transfer, 85 (2015) 852-859. https://doi.org/10.1016/j.ijheatmasstransfer.2015.02.047

[53] M. E. Nimvari, N.F. Jouybari, and Q. Esmaili, A new approach to mitigate intense temperature gradients in ceramic foam solar receivers, Renewable Energy, 122 (2018) 206-215. https://doi.org/10.1016/j.renene.2018.01.117

[54] I. Kurtbas, and N. Celik, Experimental investigation of forced and mixed convection heat transfer in a foam-filled horizontal rectangular channel, Int. J. Heat Mass Transfer, 52 (2009) 1313-1325. https://doi.org/10.1016/j.ijheatmasstransfer.2008.07.050

[55] N. Dukhan, M.A. Al-Rammahi, and A.S. Suleiman, Fluid temperature measurements inside metal foam and comparison to Brinkman–Darcy flow convection analysis, Int. J. Heat Mass Transfer, 67 (2013) 877-884. https://doi.org/10.1016/j.ijheatmasstransfer.2013.08.055

[56] W. P. Breugem, and B.-J. Boersma, Direct numerical simulations of turbulent flow over a permeable wall using a direct and a continuum approach, Phys. fluids, 17 (2005). https://doi.org/10.1063/1.1835771

[57] M. Chandesris, et al., Direct numerical simulation of turbulent heat transfer in a fluid-porous domain, Phys. Fluids, 25 (2013) 125110. https://doi.org/10.1063/1.4851416

[58] Z. Qu, H. Xu, and W. Tao, Fully developed forced convective heat transfer in an annulus partially filled with metallic foams: an analytical solution, Int. J. Heat Mass Transfer, 55 (2012) 7508-7519. https://doi.org/10.1016/j.ijheatmasstransfer.2012.07.048

[59] W. Lu, T. Zhang, and M. Yang, Analytical solution of forced convective heat transfer in parallel-plate channel partially filled with metallic foams, Int. J. Heat Mass Transfer, 100 (2016) 718-727. https://doi.org/10.1016/j.ijheatmasstransfer.2016.04.047

[60] M. E. Nimvari, M. Maerefat, and M. El-Hossaini, Numerical simulation of turbulent flow and heat transfer in a channel partially filled with a porous media, Int. J. Therm. Sci., 60 (2012) 131-141. https://doi.org/10.1016/j.ijthermalsci.2012.05.016

[61] M. Sethi, and N. Thakur, Correlations for solar air heater duct with dimpled shape roughness elements on absorber plate, Sol. Energy, 86 (2012) 2852-2861. https://doi.org/10.1016/j.solener.2012.06.024